Dynamic mortar finite element method for modeling of shear rupture on frictional rough surfaces

Citation: Tal, Yuval, and Bradford H. Hager. "Dynamic Mortar Finite Element Method for Modeling of Shear Rupture on Frictional Rough Surfaces." Computational Mechanics 61, no. 6 (September 9, 2017): 699–716.

As Published: https://doi.org/10.1007/s00466-017-1475-3

Publisher: Springer Berlin Heidelberg

Persistent URL: http://hdl.handle.net/1721.1/116382

Version: Author's final manuscript: final author's manuscript post peer review, without publisher's formatting or copy editing

Dynamic mortar finite element method for modeling of shear rupture on frictional rough surfaces

Yuval Tal[1] and Bradford H. Hager[1]

[1]*Earth Resources Laboratory, Department of Earth, Atmospheric and Planetary Sciences, Massachusetts Institute of Technology, Cambridge, Massachusetts, USA*

Abstract

This paper presents a mortar-based finite element formulation for modeling the dynamics of shear rupture on rough interfaces governed by slip-weakening (SW) and rate and state (RS) friction laws, focusing on the dynamics of earthquakes. The method utilizes the dual Lagrange multipliers and the primal–dual active set strategy concepts, together with a consistent discretization and linearization of the contact forces and constraints, and the friction laws to obtain a semi-smooth Newton method. The discretization of the RS friction law involves a procedure to condense out the state variables, thus eliminating the addition of another set of unknowns into the system. Several numerical examples of shear rupture on frictional rough interfaces demonstrate the efficiency of the method and examine the effects of the different time discretization schemes on the convergence, energy conservation, and the time evolution of shear traction and slip rate.

1. Introduction

Understanding the mechanics of shear rupture on a frictional interface is important for fields and scales ranging from earthquakes to car brakes. In this paper, we introduce a numerical method designed for studying the dynamics of shear rupture during earthquakes, focusing on the effects of the non-planar geometry and the non-linear frictional constitutive laws associated with natural faults. The method, however, can easily be adjusted for other fields and scales.

A common view is that earthquakes occur via a frictional instability, in which the frictional resistance on the fault decreases with increasing sliding or sliding velocity (see, e.g., [1]). In the context of earthquakes, the constitutive relations for the evolution of the friction coefficient can be divided into two main groups. In the group of slip-weakening (SW) friction laws, the friction coefficient evolves as a function of slip, while in the group of rate and state (RS) friction laws, it evolves as a function of sliding velocity and state variables. Many studies have examined numerically the effects of these laws on the dynamics of shear rupture during earthquakes (see, e.g., [2] and references therein). However, another source of complexity arises from the deviation of faults from planarity, which results in geometric asperities and a locally heterogeneous stress field near the fault. Map traces of the major fault systems, high-resolution maps of large continental strike-slip earthquake surface ruptures [3, 4], and measurements of roughness on exhumed faults at scales between 10 μm and 20 m [4–11] show that faults are rough at all scales and can be described as self-affine fractal surfaces.

So far, several numerical studies of dynamic rupture on rough faults governed by frictional constitutive laws have been performed [12–15]. However, these studies (as well

as the numerical studies mentioned earlier) assume that the slip on the fault is small compared to the size of the elements on the fault, thus the grid points are considered as collocated on either side of the fault during all stages of the simulation. While this assumption has a small effect for the amount of slip and the roughness bandwidth considered in these studies, it limits the minimum wavelength of roughness on the fault and may underestimate the variations of the normal stresses on the fault during slip. Therefore, a method in which the interface is governed by friction laws but also allows nonconforming meshes across the fault, with a continuous updating of the contact geometry, is needed.

The most prevalent discretization strategy in the context of large sliding contact problems is the node-to-segment (NTS) approach, in which the nodes of one surface are prohibited from penetrating the segments of the opposing surface. However, this discretization does not satisfy the contact patch test [16], where a flat contact surface should be able to exactly transmit a spatially constant contact pressure. Moreover, the non-smoothness of the discretized contact surfaces may lead to convergence difficulties and non-physical oscillations of the contact forces [17]. Therefore, although various smoothing algorithms for the NTS formulations have been proposed, segment-to-segment discretization techniques have become more attractive, especially the mortar method. The method was originally introduced in the context domain decomposition method [18] for coupling of nonconforming discretizations across interfaces. It enforces the continuity of stresses and the contact conditions across the interface in a weak integral sense, rather than as strong, pointwise constraints.

Mortar formulations for finite sliding with penalty or augmented Lagrangian

methods to enforce the contact constraints can be found in [17, 19–22]. However, the former method uses unphysical penalty parameters that can affect the accuracy and the latter method involves additional iterative procedures. The traditional direct Lagrange multiplier method avoids these drawbacks and exactly fulfills the contact constraints, but leads to an increased system of equations, with the Lagrange multipliers as additional unknowns. A remedy for this problem was given in [23], who introduced the dual spaces discretization of the Lagrange multipliers into the mortar method and enabled an efficient local elimination of the discrete Lagrange multipliers by static condensation. This concept was combined further with the primal–dual active set strategy to give an efficient semi-smooth Newton algorithm for the solution of the nonlinear system of equations [24–26]. The method was extended by [27, 28] to quasi-static finite deformation contact problems, including a consistent linearization of the contact virtual work expression and the nonlinear contact constraints. Extension to small deformation dynamic contact problems can be found in [29, 30].

Although some of the mortar formulations above include sliding on frictional interfaces, only the case of Coulomb friction with a constant coefficient of friction has been considered. In order to model shear rupture on rough frictional interfaces, this work extends the mortar formulation in [27, 28] to dynamic problems and consistently implements the SW and RS friction laws into the method. While the implementation of the SW friction law is straight forward, the implementation of the RS friction law involves a procedure to condense out the state variables, thus eliminate the addition of another set of unknowns into the system. We believe that the method provides a robust tool to study different scales of the physics of earthquakes, as well as other fields that

involve shear rupture on rough frictional interfaces. We consider in this work only a two-dimensional (2-D) model, which is quite common in dynamic simulations of the rupture process during earthquakes (see, e.g., [2, 12, 13, 15, 31] and references therein). In general, the rupture process on long strike slip faults is modeled with an antiplane framework, while that on thrust or normal faults is modeled with a plane strain framework (Mode II), assuming that there are no significant variations of the properties of the fault and medium in the perpendicular direction. In the context of the effect of roughness on the behavior of the shear rupture, the plane strain modeling is naturally more meaningful.

The remainder of the paper is organized as follows: In Section 2 we introduce the finite deformation frictional contact problem and describe the SW and RS friction laws. The corresponding weak formulation is presented in section 3. Spatial finite element discretization of the contact virtual work and contact constraints with dual Lagrange multipliers is provided in section 4. Time discretization of the resulting force equilibrium equation and discretized contact constraints is given in section 5. In Section 6, the semi-smooth Newton method for the solution of the resulting discretized system of equations is described, and the discretized form of the friction laws and their associated directional derivatives are provided. In section 7, numerical results are presented to show the accurate implementation of the friction laws, and evaluate convergence energy preservation properties for different time integration schemes. Finally, some conclusions are given in Section 8. It is important to note here that we follow the finite deformation mortar formulation of [27, 28] to make the method more general, but practically to represent the friction laws accurately small time steps have to be adopted and many of the

directional derivative calculations in the linearization of the virtual work and the normal and frictional contact constraints can be neglected.

2. Problem definition

We consider a two-dimensional contact problem with finite deformation and finite frictional sliding on an interface governed by SW or RS friction laws (Figure 1). Although only the problem of two contacting bodies is shown here, an extension to multiple bodies or fractures embedded in a continuous domain is straightforward. The initial boundary value problem is given by

$$\begin{aligned} \mathrm{Div}(\mathbf{F}\cdot\mathbf{S}) + \mathbf{b}_0 &= \rho_0\ddot{\mathbf{u}} \quad \text{in } \Omega, \\ \mathbf{u} &= \hat{\mathbf{u}}, \quad \text{on } \Gamma_u, \\ \boldsymbol{\tau} &= \hat{\boldsymbol{\tau}}, \quad \text{on } \Gamma_\sigma, \\ \mathbf{u}^0 &= \hat{\mathbf{u}}^0, \quad \text{in } \Omega_0, \\ \dot{\mathbf{u}}^0 &= \hat{\dot{\mathbf{u}}}^0, \quad \text{in } \Omega_0, \end{aligned} \tag{1}$$

where $\mathbf{F}$ is the deformation gradient tensor, $\mathbf{S}$ is the second Piola–Kirchhoff stress tensor, ρ_0 is the density in the reference configuration, $\mathbf{b}_0$ is the body load, and $\hat{\boldsymbol{\tau}}$ is the boundary traction.

In the normal direction, the Karush–Kuhn–Tucker conditions are given by

$$g_n \geq 0, \qquad \tau_n \leq 0, \qquad \tau_n g_n = 0. \tag{2}$$

Here τ_n is the normal component of the current contact tractions $\boldsymbol{\tau}_c$ and g_n is a gap function in the normal direction, defined as

$$g_n = -\mathbf{n}\left(\mathbf{x}^{(s)}\left(\mathbf{X}^{(s)}\right)\right)\cdot\left[\mathbf{x}^{(s)}\left(\mathbf{X}^{(s)}\right) - \hat{\mathbf{x}}^{(m)}\left(\hat{\mathbf{X}}^{(m)}\right)\right], \tag{3}$$

where $\hat{\mathbf{x}}^{(m)}$ is the projection of $\mathbf{x}^{(s)}$ onto the current master surface $\gamma_c^{(m)}$ along the current outward unit normal $\mathbf{n}$ and $\mathbf{X}^{(s)}$ and $\widehat{\mathbf{X}}^{(m)}$ are the corresponding points in the reference configuration (see Figure 1).

In the tangential direction, the frictional conditions with a variable friction coefficient μ are enforced by

$$\psi := |\tau_t| - \mu|\tau_n| \le 0, \qquad v_{\mathrm{t}} + \beta\tau_t = 0, \quad \beta \ge 0, \quad \psi\beta = 0. \tag{4}$$

Here τ_t is the tangential contact traction and v_{t} is tangential relative velocity defined as

$$v_{\mathrm{t}}(\mathbf{X}) = \mathbf{t}\left(\mathbf{x}^{(s)}\left(\mathbf{X}^{(s)}\right)\right) \cdot \left[\dot{\mathbf{x}}^{(s)}\left(\mathbf{X}^{(s)}\right) - \dot{\hat{\mathbf{x}}}^{(m)}\left(\widehat{\mathbf{X}}^{(m)}\right)\right], \tag{5}$$

where $\mathbf{t}$ is the current unit tangential vector.

2.1. Slip-weakening friction

In the simple SW friction law [32–34] the coefficient of friction μ drops linearly from its static value, μ_s, to its sliding value, μ_d, over a specified distance, d_c, (Fig. 2a).

$$\mu = \begin{cases} \mu_s + \dfrac{\mu_d - \mu_s}{d_c} u_t, & u_t \le d_c \\ \mu_d, & u_t > d_c \end{cases}, \tag{6}$$

where u_t is the tangential relative slip along the contact. More complicated slip based friction laws that may also include an initial stage of hardening and then exponential decay of the friction coefficient with slip were also suggested [35, 36]. We consider here only the simple SW friction law, but the other slip-based laws can be implemented in a similar way.

2.2. Rate and state friction

The response of the friction coefficient to a change in sliding velocity is shown schematically in Figure 2b. This behavior was observed experimentally for many

materials [37] and is the basis of the empirical RS friction laws of [37, 38]. With a sudden increase in sliding velocity there is an instantaneous increase of the friction coefficient followed by an evolution stage, in which it decreases to a new steady-state value. These behavior is governed by two material property constants a and b, respectively. Frictional instability can occur only if the steady-state velocity dependence in friction coefficient is velocity weakening, i.e. $a - b < 0$.

Several variations of RS friction laws have been proposed, but the aging law is in the best agreement with experimental observations [1, 39]. In this form of the law, the friction coefficient evolves as

$$\mu = \mu^* + a\ln\left(\frac{v_t}{v^*}\right) + b\ln\left(\frac{v^*\theta}{L}\right), \tag{7}$$

where v^* is a reference velocity, μ^* the steady-state friction at $v_t = v^*$, L is the critical slip distance, and θ is a state variable governed by an aging law as

$$\dot{\theta} = 1 - \frac{\theta v_t}{L}, \tag{8}$$

On the micro scale, θ is interpreted as the average age of contacts and L as the slip necessary to renew surface contacts [37].

3. Weak form

Using appropriate spaces for the displacements $\mathbf{u}$ and virtual displacements $\boldsymbol{\delta}\mathbf{u}$, the virtual work expression is given by

$$\delta\Pi(\mathbf{u}, \delta\mathbf{u}) = \delta\Pi_{\text{int,ext}}(\mathbf{u}, \delta\mathbf{u}) + \delta\Pi_{\text{c}}(\mathbf{u}, \delta\mathbf{u}). \tag{9}$$

where $\delta\Pi_{\text{int,ext}}(\mathbf{u}, \delta\mathbf{u})$ is the standard virtual work from internal and external forces and $\delta\Pi_{\text{c}}(\mathbf{u}, \delta\mathbf{u})$ the contact virtual work. We use the total Lagrangian formulation of [40] to compute $\delta\Pi_{\text{int,ext}}$. Exploiting the balance of linear momentum across the contact

interface and introducing Lagrange multipliers $\boldsymbol{\lambda} = -\boldsymbol{\tau}_c$ on the "slave" side of the contact, the contact virtual work is expressed as

$$\delta\Pi_{\mathrm{c}} = \int_{\gamma_c^{(s)}} \boldsymbol{\lambda} \cdot \left(\delta\mathbf{u}^{(1)} - \delta\mathbf{u}^{(2)}\right) d\gamma. \tag{10}$$

In the normal direction, the Karush–Kuhn–Tucker conditions are enforced in a weak integral form and point wise as

$$\int_{\gamma_c^{(s)}} \delta\lambda_n g_n d\gamma \geq 0, \qquad \lambda_n \geq 0, \qquad \lambda_n g_n = 0, \tag{11}$$

In the tangential direction, the frictional conditions are given by

$$\begin{gathered} \int_{\gamma_c^{(s)}} \delta\lambda_t \left(v_{\mathrm{t,rel}} - \beta_{co}\lambda_t\right) d\gamma = 0, \\ \psi := |\lambda_t| - \mu|\lambda_n| \leq 0, \qquad \beta_{co} \geq 0, \quad \psi\beta_{co} = 0 \end{gathered} \tag{12}$$

4. Finite element spatial discretization

The geometry, displacements, and displacement time derivatives of the contacting slave and master surfaces are discretized with standard finite element shape functions as

$$\mathbf{u}^{(1)}|_{\gamma_c^{(1)}} = \sum_{j=1}^{n_{sl}} N_j \mathbf{d}_j\,, \qquad \mathbf{u}^{(2)}|_{\gamma_c^{(2)}} = \sum_{j=1}^{n_{mas}} N_l \mathbf{d}_l, \tag{13}$$

where n_{sl} and where n_{mas} are the numbers of nodes on the slave surface on the slave surface $\gamma_c^{(1)}$ and master surface $\gamma_c^{(2)}$.

For the interpolation of the Lagrange multiplier field, dual shape functions $\boldsymbol{\phi}_j$ are introduced on the slave surface as

$$\lambda = \sum_{j=1}^{n_{sl}} \boldsymbol{\phi}_j \boldsymbol{\lambda}_j, \tag{14}$$

where $\boldsymbol{\lambda}_j$ are the discrete nodal Lagrange multipliers. These shape functions fulfill the so-called biorthogonality condition [23] as

$$\int_{\gamma_c^{(1)}} \phi_j N_k^{(1)} d\gamma = \delta_{ij} \int_{\gamma_c^{(1)}} N_k^{(1)} d\gamma. \tag{15}$$

A detailed description regarding the construction of the dual shape functions is given in [27, 41]. Substituting (13 – 15) into (10) leads to the discrete vector of contact forces

$$\mathbf{f}_{\mathrm{c}}(\mathbf{d}, \boldsymbol{\lambda}) = [0, -\mathbf{M}_M, \mathbf{D}_S]^T \boldsymbol{\lambda}. \tag{16}$$

Where $\mathbf{D}_S \in \mathbb{R}^{2n_{sl} \times 2n_{sl}}$ and $\mathbf{M}_M \in \mathbb{R}^{2n_{sl} \times 2n_{mas}}$ are coupling matrices arising from the mortar integrals (see appendix A). The biorthogonality condition results in a diagonal matrix $\mathbf{D}_S$, which allows static condensation of the discrete Lagrange multipliers and simplifies the linearization and solution process.

Substituting (16) into (9), the algebraic form of the force equilibrium equation is given by

$$\mathbf{M}\ddot{\mathbf{d}} + \mathbf{f}_{\mathrm{int}}(\mathbf{d}) + \mathbf{f}_{\mathrm{c}}(\mathbf{d}, \boldsymbol{\lambda}) - \mathbf{f}_{\mathrm{ext}} = 0, \tag{17}$$

where $\mathbf{M}$ represents the mass matrix, $\mathbf{f}_{\mathrm{int}}(\mathbf{d})$ is the vector of the deformation dependent internal forces, and $\mathbf{f}_{\mathrm{ext}}$ is the vector of external forces.

As shown in [27], the discretized form of the normal conditions in (11) is equivalent to the following set of pointwise conditions

$$\tilde{g}_{nj} \geq 0, \qquad \lambda_{nj} \geq 0, \qquad \lambda_{nj} \tilde{g}_{nj} = 0, \tag{18}$$

where the discrete weight gap function in the normal direction is given by

$$\tilde{g}_{nj} = -\mathbf{n}_j^T \mathbf{D}_S[j,j] \mathbf{x}_j^{(s)} + \mathbf{n}_j^T \sum_{l=1}^{n_{mas}} \mathbf{M}_M[j,l] \, \mathbf{x}_l^{(m)}. \tag{19}$$

Following [28], the nodal tangential contact conditions are given by

$$\psi_j \coloneqq |\lambda_{tj}| - \mu_j |\lambda_{nj}| \leq 0, \qquad \tilde{v}_{\mathrm{tj}} - \tilde{\beta}_j \lambda_{tj} = 0, \quad \tilde{\beta}_j \geq 0, \quad \psi_j \tilde{\beta}_j = 0, \tag{20}$$

with the weighted tangential relative velocity defined as

$$\tilde{v}_{\mathrm{tj}} = \mathbf{t}_j^T \mathbf{D}_S[j,j] \dot{\mathbf{x}}_j^{(s)} - \mathbf{t}_j^T \sum_{l=1}^{n_{mas}} \mathbf{M}_M[j,l]\, \dot{\mathbf{x}}_l^{(m)}, \tag{21}$$

and

$$\tilde{\beta}_j = \int_{\gamma_c^{(1)}} \phi_j d\gamma \beta_j. \tag{22}$$

It is important to note that the definition of the weighted tangential relative velocity here is slightly different from that of [28], who used the time derivatives of $\mathbf{D}_S$ and $\mathbf{M}_M$ to guarantee frame indifference also for large rotations during a given time step. In this study this effect is negligible because the displacements during the time steps must be maintained small in order to accurately model the evolution of the frictional stress with slip or slip rate. Moreover, we do not aim in this study to address problems with very large rotation.

5. Time discretization

The force equilibrium equation is discretized in time with the Hilber-Hughes-Taylor (HHT) scheme [42] as following

$$\mathbf{r} = \mathbf{M}\ddot{\mathbf{d}}^{t+\Delta t} + \mathbf{f}_{int}(\mathbf{d}^{t+\alpha}) + \mathbf{f}_c\left(\mathbf{d}^{t+\alpha}, \boldsymbol{\lambda}^{t+\hat{\alpha}}\right) - \mathbf{f}_{ext}^{t+\alpha}, \tag{23.a}$$

$$\mathbf{d}^{t+\alpha} = (1-\alpha)\mathbf{d}^t + \alpha \mathbf{d}^{t+1}, \tag{23.b}$$

$$\dot{\mathbf{d}}^{t+\alpha} = (1-\alpha)\dot{\mathbf{d}}^t + \alpha \dot{\mathbf{d}}^{t+1} = (1-\alpha)\dot{\mathbf{d}}^t + \alpha\left(\frac{\mathbf{d}^{t+1} - \mathbf{d}^t}{\Delta t \beta/\gamma} - \frac{1-\beta/\gamma}{\beta/\gamma}\dot{\mathbf{d}}^t\right) \tag{23.c}$$

$$= \frac{\alpha}{\beta/\gamma}\frac{\mathbf{d}^{t+1} - \mathbf{d}^t}{\Delta t} + \frac{\beta/\gamma - \alpha}{\beta/\gamma}\dot{\mathbf{d}}^t,$$

$$\ddot{\mathbf{d}}^{t+1} = \frac{\dot{\mathbf{d}}^{t+1} - \dot{\mathbf{d}}^{t}}{\gamma \Delta t} - \frac{1-\gamma}{\gamma}\ddot{\mathbf{d}}^{t} = \frac{\mathbf{d}^{t+1} - \mathbf{d}^{t}}{\beta \Delta t^2} - \frac{1}{\beta \Delta t}\dot{\mathbf{d}}^{t} - \left(\frac{1}{\gamma} - 1\right)\ddot{\mathbf{d}}^{t}. \tag{23.d}$$

In general, a term with the superscript $t + \alpha$ is discretized as in (23.b), while a term with the superscript $t + \hat{\alpha}$ is the actual value calculated at time $t + \alpha$. Substituting (23.d) in (23.a) to eliminate the accelerations gives

$$\mathbf{r} = \frac{1}{\beta \Delta t^2}\mathbf{M}\mathbf{d}^{t+\Delta t} + \mathbf{f}_{int}(\mathbf{d}^{t+\alpha}) + \mathbf{f}_c\left(\mathbf{d}^{t+\alpha}, \boldsymbol{\lambda}^{t+\hat{\alpha}}\right) - \mathbf{f}_{ext}^{t+\alpha} - \mathbf{R}, \tag{24}$$

where

$$\mathbf{R} = \mathbf{M}\left[\frac{1}{\beta \Delta t^2}\mathbf{d}^{t} + \frac{1}{\beta \Delta t}\dot{\mathbf{d}}^{t} + \left(\frac{1}{\gamma} - 1\right)\ddot{\mathbf{d}}^{t}\right]. \tag{25}$$

Note that the scheme reduces to the family of Newmark integration schemes [43] for $\alpha = 1$ and to the midpoint rule for $\alpha = 1/2$, $\beta = 1/2$, and $\gamma = 1$. Focusing on the contact, we consider here only linear elastic materials, thus the computation of $\mathbf{f}_{\text{int}}(\mathbf{d}^{t+\alpha})$ is straightforward; an extension to other elastic materials is provided in [44, 45]. The contact force time discretization is approximated as $\mathbf{f}_c\left(\mathbf{d}^{t+\alpha}, \boldsymbol{\lambda}^{t+\hat{\alpha}}\right) = [0, -\mathbf{M}_M^{t+\alpha}, \mathbf{D}_S^{t+\alpha}]^T \boldsymbol{\lambda}^{t+\hat{\alpha}}$.

Following [46], to conserve energy in dynamic simulations, we enforce the persistency condition in the normal direction as

$$\begin{gathered} \tilde{g}_{nj}^{t} > 0 \implies \lambda_{nj}^{t+\hat{\alpha}} = 0, \\ \tilde{g}_{nj}^{t} \leq 0 \implies \dot{\tilde{g}}_{nj}^{t+\alpha} \geq 0, \qquad \lambda_{nj}^{t+\hat{\alpha}} \geq 0, \qquad \lambda_{nj}^{t+\hat{\alpha}} \dot{\tilde{g}}_{nj}^{t+\alpha} = 0, \end{gathered} \tag{26}$$

with the gap rate in the normal direction defined as

$$\dot{\tilde{g}}_{nj}^{t+\hat{\alpha}} = -\left(\mathbf{n}_j^{t+\alpha}\right)^T \mathbf{D}_S^{t+\alpha}[j,j]\dot{\mathbf{d}}_j^{t+\alpha} + \left(\mathbf{n}_j^{t+\alpha}\right)^T \sum_{l=1}^{n_{mas}} \mathbf{M}_M^{t+\alpha}[j,l]\,\dot{\mathbf{d}}_l^{t+\alpha}. \tag{27}$$

This set of conditions ensures that the expression $\lambda_{nj}^{t+\hat{\alpha}}\dot{\tilde{g}}_{nj}^{t+\alpha}=0$ holds also at time steps when nodes come into contact or are released, thus the contact energy in the normal direction is always zero. However, it is important to note that this formulation of the constraints may result in small penetrations, especially for relatively large time steps. An energy-conserving scheme that naturally enforce the standard Kuhn–Tucker contact conditions at entire time steps is introduced by [47], but with a penalty technique for the contacts. A discussion on the additional computational cost associated with the mortar formulation in the case of large deformation dynamic problems, as well as a remedy to the problem, is given in [48].

In the tangential direction, the frictional conditions are enforced at time $t+\alpha$ as

$$\begin{aligned}\psi_j^{t+\hat{\alpha}} &:= \left|\lambda_{tj}^{t+\hat{\alpha}}\right| - \mu_j^{t+\hat{\alpha}}\left|\lambda_{nj}^{t+\hat{\alpha}}\right| \le 0,\\ &\tilde{v}_{tj}^{t+\hat{\alpha}} - \tilde{\beta}_j^{t+\hat{\alpha}} z_{tj}^{t+\hat{\alpha}} = 0, \quad \tilde{\beta}_j^{t+\hat{\alpha}} \ge 0, \quad \psi_j^{t+\hat{\alpha}}\tilde{\beta}_j^{t+\hat{\alpha}} = 0,\end{aligned} \tag{28}$$

where

$$\tilde{v}_{tj}^{t+\hat{\alpha}} = \left(\mathbf{t}_j^{t+\alpha}\right)^T \mathbf{D}_S^{t+\alpha}[j,j]\dot{\mathbf{d}}_j^{t+\alpha} - \left(\mathbf{t}_j^{t+\alpha}\right)^T \sum_{l=1}^{n_{mas}} \mathbf{M}_M^{t+\alpha}[j,l]\,\dot{\mathbf{d}}_l^{t+\alpha}. \tag{29}$$

In the case of RS friction, $\tilde{v}_{nj}^{t+\hat{\alpha}}$ and $\mu_j^{t+\hat{\alpha}}$ involve the calculation of nodal velocities also in a quasi-static formulation. In this case one would omit the acceleration term in (23.a) and take $\alpha=1$ and $\beta/\gamma=1$, to obtain a backward Euler scheme.

6. Solution with a semi-smooth Newton method

Aiming to obtain a Newton-type algorithm for the solution of the discretized system of nonlinear algebraic equations in (24), (26), and (28), the concept of dual Lagange multipliers is combined with the primal-dual active set strategy and the contact

conditions in (26) and (28) are replaced by equivalent nonlinear semi-smooth complementarity (NCP) functions equations. These functions reformulate these conditions as equality conditions that enable the treatment of all sources of nonlinearities in a single iterative scheme, including the categorization of all potential contact nodes into not in contact, sticking, and slipping nodes.

6.1. Non-smooth complementarity functions

Similarly to [24, 25, 27, 28], the complementarity functions for the normal and tangential conditions are defined for each slave node $j \in S$ as

$$C_{nj}\left(\boldsymbol{\lambda}_j^{t+\hat{\alpha}}, \mathbf{d}^{t+\alpha}\right) = \lambda_{nj}^{t+\hat{\alpha}} - \max\left\{0, \lambda_{nj}^{t+\hat{\alpha}} - c_n \tilde{g}_j^{test}\right\} = 0 \tag{30}$$

and

$$\begin{aligned} C_{tj}\left(\boldsymbol{\lambda}_j^{t+\hat{\alpha}}, \mathbf{d}^{t+\alpha}\right) &= \max\left(\mu_j^{t+\hat{\alpha}}\left(\lambda_{nj}^{t+\hat{\alpha}} - c_n \tilde{g}_j^{test}\right), \left|\lambda_{tj}^{t+\hat{\alpha}} + c_t \tilde{v}_{tj}^{t+\hat{\alpha}}\right|\right)\lambda_{tj}^{t+\hat{\alpha}} \\ &- \mu_j^{t+\hat{\alpha}} \max\left(0, \left(\lambda_{nj}^{t+\hat{\alpha}} - c_n \tilde{g}_j^{test}\right)\right)\left(\lambda_{tj}^{t+\hat{\alpha}} + c_t \tilde{v}_{tj}^{t+\hat{\alpha}}\right) = 0, \quad c_t > 0, \end{aligned} \tag{31}$$

respectevely, where $\tilde{g}_j^{test}$ in (30) is defined as

$$\tilde{g}_j^{test} := \begin{cases} \dfrac{\lambda_{nj}^{t+\hat{\alpha}}}{c} + \tilde{g}_{nj}^{t} & \text{if} \quad \tilde{g}_{nj}^{t} > 0 \\ \dot{\tilde{g}}_{nj}^{t+\hat{\alpha}} \Delta t & \text{if} \quad \tilde{g}_{nj}^{t} \leq 0 \end{cases}.$$

The algorithmic parameters c_n and c_t do not affect the accuracy, but to achive a good convergence behavior, they should be on the order of $E\Delta t / l_{slave}$, where E is the Young's modulus of the medium near the fault and l_{slave} is the average length of the slave elements. Note that in a quasi-static formulation $(\alpha = 1)$, the complementarity functions

should involve the normal gap function rather than its rate, thus $\tilde{g}_j^{test} = \tilde{g}_{nj}^{t+1}$.

6.2. Consistent linearization within the semi-smooth Newton method

To solve $\mathbf{d}^{t+\Delta t}, \mathbf{z}^{t+\hat{\alpha}}$, an iterative semi-smooth Newton method is applied to the nonlinear system of equations of (24), (30) and (31) as

$$\Delta\mathbf{r}\left({}^{k}\mathbf{d}^{t+\alpha},\ {}^{k}\boldsymbol{\lambda}^{t+\hat{\alpha}}\right) = -\,{}^{k}\mathbf{r}^{t+\hat{\alpha}}, \tag{32.a}$$

$$\Delta C_{nj}\left({}^{k}\mathbf{d}^{t+\alpha},\ {}^{k}\boldsymbol{\lambda}^{t+\hat{\alpha}}\right) = -\,{}^{k}C_{nj}^{t+\hat{\alpha}} \quad \forall j \in S, \tag{32.b}$$

$$\Delta C_{tj}\left({}^{k}\mathbf{d}^{t+\alpha},\ {}^{k}\boldsymbol{\lambda}^{t+\Delta\hat{\alpha}}\right) = -\,{}^{k}C_{tj}^{t+\hat{\alpha}} \quad \forall j \in S, \tag{32.c}$$

with the update

$${}^{k+1}\mathbf{d}^{t+1} = {}^{k}\mathbf{d}^{t+1} + \Delta\,{}^{k}\mathbf{d}^{t+1}, \qquad {}^{k+1}\boldsymbol{\lambda}^{t+\hat{\alpha}} = {}^{k}\boldsymbol{\lambda}^{t+\hat{\alpha}} + \Delta\,{}^{k}\boldsymbol{\lambda}^{t+\hat{\alpha}}, \tag{33}$$

where the superscript ${}^{\cdot k+1}$ stands for the current iteraion.

The linearization of the force equilibrium in (32.a) is given in Appendix B. We linearize (32.b) and (32.c) similarly to [27, 28], but account for a variable friction coefficient and dynamic time discretization. In the normal direction, (30 and 32.b) yield the separation of the slave nodes into an inactive node set ${}^{k}I$ and an active node set ${}^{k}A$ as

$$\begin{aligned} {}^{k}I &:= \left\{ j \in |\ {}^{k}\lambda_{nj}^{t+\hat{\alpha}} - c_n\,{}^{k}\tilde{g}_j^{test} \le 0 \right\} \\ {}^{k}A &:= \left\{ j \in |\ {}^{k}\lambda_{nj}^{t+\hat{\alpha}} - c_n\,{}^{k}\tilde{g}_j^{test} > 0 \right\}, \end{aligned} \tag{34}$$

which leads to [25, 27]

$$\begin{cases} {}^{k+1}\boldsymbol{\lambda}_j^{t+\hat{\alpha}} = 0 & \forall j \in {}^{k}I \\ \Delta\,{}^{k}\dot{\tilde{g}}_{nj}^{t+\hat{\alpha}} = -\,{}^{k}\dot{\tilde{g}}_{nj}^{t+\hat{\alpha}} & \forall j \in {}^{k}A \end{cases}, \tag{35.a}$$

(35.b)

where the directional derivative of the gap function is given in Appendix B.

In the tangential direction, the directional derivative of (31) also splits the slave nodes into inactive and active node sets defined in (34), with algebraic representation of (35.a) for the inactive node set. Similarly to [25, 28], the active node set branches into a stick node set ${}^{k}St$ and a slip node set ${}^{k}Sl$ as

$$\begin{aligned} {}^{k}St &:= \left\{ j \in {}^{k}A \middle| \left| \left({}^{k}\lambda_{tj}^{t+\hat{\alpha}} + c_t \, {}^{k}\tilde{v}_{tj}^{t+\hat{\alpha}} \right) \right| - {}^{k}\mu_j^{t+\hat{\alpha}} \left({}^{k}\lambda_{nj}^{t+\hat{\alpha}} - c_n \tilde{g}_j^{test} \right) < 0 \right\} \\ {}^{k}Sl &:= \left\{ j \in {}^{k}A \middle| \left| \left({}^{k}\lambda_{tj}^{t+\hat{\alpha}} + c_t \, {}^{k}\tilde{v}_{tj}^{t+\hat{\alpha}} \right) \right| - {}^{k}\mu_j^{t+\hat{\alpha}} \left({}^{k}\lambda_{nj}^{t+\hat{\alpha}} - c_n \tilde{g}_j^{test} \right) \geq 0 \right\}. \end{aligned} \tag{36}$$

The directional derivatives of (31.c) for the sticking and slipping nodes are given in Appendix B. They involve the discretized form of coefficient of friction and its directional derivative. In the following sections we derive the numerical approximation of these quantities for SW and RS friction laws.

6.2.1. Slip-weakening friction

The discrete form of the SW friction law given in (6) for a node *j* on the slave surface is given by

$${}^{\boldsymbol{k}}\mu_j^{t+\hat{\alpha}} = \begin{cases} \mu_s + \dfrac{\mu_d - \mu_s}{d_c} \, {}^{\boldsymbol{k}}u_{rel,j}^{t+\hat{\alpha}}, & {}^{\boldsymbol{k}}u_{rel,j}^{t+\hat{\alpha}} \leq d_c \\ \mu_d, & {}^{\boldsymbol{k}}u_{rel,j}^{t+\hat{\alpha}} > d_c \end{cases}. \tag{37}$$

with the total relative slip of node *j* on the slave surface ${}^{\boldsymbol{k}}u_{rel,j}^{t+\hat{\alpha}}$ defined as

$$\begin{aligned} {}^{\boldsymbol{k}}u_{rel,j}^{t+\hat{\alpha}} &= u_{rel,j}^{t} + {}^{\boldsymbol{k}}\mathbf{t}_j^{t+\alpha} \cdot \left[\left({}^{\boldsymbol{k}}\mathbf{d}_j^{t+\alpha} - \mathbf{d}_j^{t} \right) - \left({}^{\boldsymbol{k}}\hat{\mathbf{d}}_j^{t+\alpha} - \hat{\mathbf{d}}_j^{t} \right) \right] \\ &= u_{rel,j}^{t} + {}^{\boldsymbol{k}}\mathbf{t}_j^{t+\alpha} \cdot \left[\left({}^{\boldsymbol{k}}\mathbf{d}_j^{t+\alpha} - \mathbf{d}_j^{t} \right) - \sum_{l=1}^{2} {}^{\boldsymbol{k}}N_l^{t+\alpha} \left({}^{\boldsymbol{k}}\mathbf{d}_l^{t+\alpha} - \mathbf{d}_l^{t} \right) \right] \\ &= u_{rel,j}^{t} + {}^{\boldsymbol{k}}\mathbf{t}_j^{t+\alpha} \\ &\cdot \left[\left({}^{\boldsymbol{k}}\mathbf{d}_j^{t+\alpha} - \mathbf{d}_j^{t} \right) - \sum_{l=1}^{n_{mas}} {}^{\boldsymbol{k}}\mathbf{N}^{t+\alpha}[j,l] \left({}^{\boldsymbol{k}}\mathbf{d}_l^{t+\alpha} - \mathbf{d}_l^{t} \right) \right], \end{aligned} \tag{38}$$

where $\hat{\mathbf{d}}_j$ is the displacement of node $\hat{\mathbf{x}}_j$ corresponding to the projection of the slave node on the master surface (see Figure 1), $\mathbf{d}_l$ is the displacement of the nodes associated with a surface element that includes $\hat{\mathbf{x}}_j$, $N_1 = 0.5\left(1 - \xi\left(\hat{\mathbf{x}}_j\right)\right)$ and $N_2 = 0.5\left(1 + \xi\left(\hat{\mathbf{x}}_j\right)\right)$ are the corresponding shape functions, and $\mathbf{N}$ is a matrix defined as $\mathbf{N}[j,l] = \left(N_{1jl+}N_{2jl}\right)\mathbf{I}$.

The directional derivative of (37) is given by

$$\Delta\, {}^{k}\mu_j^{t+\hat{\alpha}} = \begin{cases} \dfrac{\mu_d - \mu_s}{d_c}\Delta\left({}^{k}u_{rel,j}^{t+\hat{\alpha}}\right), & u_{rel,j}^{t+\hat{\alpha}} \le d_c \\ 0, & u_{rel,j}^{t+\hat{\alpha}} > d_c \end{cases}, \tag{39}$$

where

$$\begin{aligned} \Delta\left({}^{k}u_{rel,j}^{t+\hat{\alpha}}\right) = {}& {}^{k}\mathbf{t}_j^{t+\alpha} \cdot \left[\alpha\Delta\, {}^{k}\mathbf{d}_j^{t+1} - \sum_{l=1}^{n_{mas}} {}^{k}\mathbf{N}^{t+\alpha}[j,l]\alpha\Delta\, {}^{k}\mathbf{d}_l^{t+1}\right] \\ & + \alpha\Delta\, {}^{k}\mathbf{t}_j^{t+1} \cdot \left[\left({}^{k}\mathbf{d}_j^{t+\alpha} - \mathbf{d}_j^{t}\right) - \sum_{l=1}^{n_{mas}} {}^{k}\mathbf{N}^{t+\alpha}[j,l]\left({}^{k}\mathbf{d}_l^{t+\alpha} - \mathbf{d}_l^{t}\right)\right] \\ & + {}^{k}\mathbf{t}_j^{t+\alpha} \cdot \left[-\sum_{l=1}^{n_{mas}} \alpha\Delta\, {}^{k}\mathbf{N}^{t+1}[j,l]\left({}^{k}\mathbf{d}_l^{t+\Delta t} - \mathbf{d}_l^{t}\right)\right]. \end{aligned} \tag{40}$$

The directional derivative ΔN_l involves the directional derivative of $\xi\left(\hat{\mathbf{x}}_j\right)$, which is given in [27].

6.2.2. Rate and state friction

The discrete form of the RS friction law (7 and 8) for node *j* on the slave surface is given by

$${}^{k}\mu_j^{t+\hat{\alpha}} = \mu^* + a\ln\left(\frac{{}^{k}\dot{u}_{rel,j}^{t+\hat{\alpha}} + v_{th}}{v^*}\right) + b\ln\left(\frac{{}^{k}\theta_j^{t+\alpha}}{\theta^*}\right). \tag{41}$$

with the state variable evolving as

$$ {}^{k}\dot{\theta}_j^{t+\alpha} = 1 - \frac{{}^{k}\theta_j^{t+\alpha}\left({}^{k}\dot{u}_{rel,j}^{t+\hat{\alpha}} + v_{th} \right)}{L} \tag{42} $$

and the slip rate defined as

$$ {}^{k}\dot{u}_{rel,j}^{t+\hat{\alpha}} = {}^{k}\mathbf{t}_j^{t+\alpha} \cdot \left[{}^{k}\dot{\mathbf{d}}_j^{t+\alpha} - \sum_{l=1}^{n_{mas}} {}^{k}\mathbf{N}^{t+\alpha}[j,l] \, {}^{k}\dot{\mathbf{d}}_l^{t+\alpha} \right]. \tag{43} $$

The threshold velocity term, v_{th}, is added to avoid singularity at slip rate of $\dot{u}_{rel,j}^{t+\hat{\alpha}} = 0$.

The directional derivative of (41) is simply

$$ \Delta\mu^{t+\hat{\alpha}} = \frac{a}{{}^{k}\dot{u}_{rel,j}^{t+\hat{\alpha}} + v_{th}} \Delta \, {}^{k}\dot{u}_{rel,j}^{t+\hat{\alpha}} + \frac{b}{{}^{k}\theta_j^{t+\alpha}} \Delta\theta_j^{t+\alpha}, \tag{44} $$

with the directional derivative of the slip rate given by

$$ \begin{aligned} \Delta \, {}^{k}\dot{u}_{rel,j}^{t+\hat{\alpha}} = {} & {}^{k}\mathbf{t}_j^{t+\alpha} \cdot \left[\alpha\Delta \, {}^{k}\dot{\mathbf{d}}_j^{t+1} - \sum_{l=1}^{n_{mas}} {}^{k}\mathbf{N}^{t+\alpha}[j,l] \Delta \, {}^{k}\dot{\mathbf{d}}_l^{t+\alpha} \right] \\ & + \alpha\Delta \, {}^{k}\mathbf{t}_j^{t+1} \cdot \left[{}^{k}\dot{\mathbf{d}}_j^{t+\alpha} - \sum_{l=1}^{n_{mas}} {}^{k}\mathbf{N}^{t+\alpha}[j,l] \, {}^{k}\dot{\mathbf{d}}_l^{t+\alpha} \right] \\ & + {}^{k}\mathbf{t}_j^{t+\alpha} \cdot \left[- \sum_{l=1}^{n_{mas}} \alpha\Delta \, {}^{k}\mathbf{N}^{t+1}[j,l] \, {}^{k}\dot{\mathbf{d}}_l^{t+\alpha} \right]. \end{aligned} \tag{45} $$

Similarly to [49], to avoid an additional set of variables, we aim to express ${}^{k}\theta_j^{t+\alpha}$ and $\Delta \, {}^{k}\theta_j^{t+\alpha}$ as a function of the slip rate. We discretize the state variable in time similar to the nodal displacement and velocity time discretization in (23):

$$ {}^{k}\theta_j^{t+\alpha} = (1-\alpha)\theta_j^{t} + \alpha\theta_j^{t+1}, \tag{46.a} $$

$$ {}^{k}\dot{\theta}_j^{t+\alpha} = \frac{\alpha}{\beta/\gamma} \frac{{}^{k}\theta_j^{t+1} - \theta_j^{t}}{\Delta t} + \frac{\beta/\gamma - \alpha}{\beta/\gamma} \dot{\theta}_j^{t}, \tag{46.b} $$

Equating (46.b) with (42) together with some algebra gives

$$ {}^{k}\theta_j^{t+\alpha} = \left[1 + \frac{\theta_j^t}{(\beta/\gamma)\Delta t} - \frac{\beta/\gamma - \alpha}{\beta/\gamma}\dot{\theta}_j^t\right] \frac{(\beta/\gamma)L\Delta t}{L + (\beta/\gamma)\Delta t\left({}^{k}\dot{u}_{rel,j}^{t+\hat{\alpha}} + v_{th}\right)} \tag{47} $$

and

$$ \begin{aligned} \Delta\,{}^{k}\theta_j^{t+\alpha} = -\Bigg[1 + \frac{1}{\beta/\gamma}\frac{\theta_j^t}{\Delta t} \\ - \frac{\beta/\gamma - \alpha}{\beta/\gamma}\dot{\theta}_j^t\Bigg] \frac{(\beta/\gamma)^2 L(\Delta t)^2}{\left(L + (\beta/\gamma)\Delta t\left({}^{k}\dot{u}_{rel,j}^{t+\hat{\alpha}} + v_{th}\right)\right)^2} \Delta\,{}^{k}\dot{u}_{rel,j}^{t+\hat{\alpha}}. \end{aligned} \tag{48} $$

6.3 Algebraic representation

Finally, the global algebraic representation of (32) to be solved in each iteration is derived. The matrix and vector blocks of this linear system are defined by the five sets *N*, *M*, *I*, *St* and *Sl*. We drop the iteration and time indices here for ease of notation.

$$ \begin{bmatrix} \mathbf{K}_{NN} & \mathbf{K}_{NM} & \mathbf{K}_{NI} & \mathbf{K}_{NSt} & \mathbf{K}_{NSl} & 0 & 0 & 0 \\ \mathbf{K}_{MN} & \widetilde{\mathbf{K}}_{MM} & \widetilde{\mathbf{K}}_{MI} & \widetilde{\mathbf{K}}_{MSt} & \widetilde{\mathbf{K}}_{MSl} & -\mathbf{M}_{MI}^T & -\mathbf{M}_{MSt}^T & -\mathbf{M}_{MSl}^T \\ \mathbf{K}_{IN} & \widetilde{\mathbf{K}}_{IM} & \widetilde{\mathbf{K}}_{II} & \widetilde{\mathbf{K}}_{ISt} & \widetilde{\mathbf{K}}_{ISl} & \mathbf{D}_{SI} & 0 & 0 \\ \mathbf{K}_{StN} & \widetilde{\mathbf{K}}_{StM} & \widetilde{\mathbf{K}}_{StI} & \widetilde{\mathbf{K}}_{StSt} & \widetilde{\mathbf{K}}_{StSl} & 0 & \mathbf{D}_{SSt} & 0 \\ \mathbf{K}_{SlN} & \widetilde{\mathbf{K}}_{SlM} & \widetilde{\mathbf{K}}_{SlI} & \widetilde{\mathbf{K}}_{SlSt} & \widetilde{\mathbf{K}}_{SlSl} & 0 & 0 & \mathbf{D}_{SSl} \\ 0 & 0 & 0 & 0 & 0 & \mathbf{I}_I & 0 & 0 \\ 0 & \mathbf{S}_{AM} & \mathbf{S}_{AI} & \mathbf{S}_{ASt} & \mathbf{S}_{Al} & 0 & 0 & 0 \\ 0 & \mathbf{F}_{StM} & \mathbf{F}_{StI} & \mathbf{F}_{StSt} & \mathbf{F}_{StSl} & 0 & \mathbf{P}_{St} & 0 \\ 0 & \mathbf{G}_{SlM} & \mathbf{G}_{SlI} & \mathbf{G}_{SlSt} & \mathbf{G}_{SlSl} & 0 & 0 & \mathbf{L}_{Sl} \end{bmatrix} \begin{bmatrix} \Delta\mathbf{d}_N \\ \Delta\mathbf{d}_M \\ \Delta\mathbf{d}_I \\ \Delta\mathbf{d}_{St} \\ \Delta\mathbf{d}_{Sl} \\ \boldsymbol{\lambda}_I \\ \boldsymbol{\lambda}_{St} \\ \boldsymbol{\lambda}_{Sl} \end{bmatrix} = - \begin{bmatrix} \mathbf{r}_N \\ \mathbf{r}_M \\ \mathbf{r}_I \\ \mathbf{r}_{St} \\ \mathbf{r}_{Sl} \\ 0 \\ \mathbf{g}_{nA} \\ \mathbf{C}_{t,St} \\ \mathbf{C}_{t,Sl} \end{bmatrix} \tag{49} $$

The first five rows can be identified as the linearized algebraic form of the force equilibrium equation in (32.a), where $\widetilde{\mathbf{K}} = \mathbf{K} + \tilde{\mathbf{C}}$. The sixth row represents the contact constraint condition for nodes of the inactive set *I*. In the seventh row, matrix $\mathbf{S}_A \in \mathbb{R}^{n_a \times (2n_{mas}+2n_{sl})}$ is the assembly of all linearizations of $\mathbf{g}_{nA}$ (32.b, 35.b), where n_a is the number of active slave nodes. In the eighth row, $\mathbf{F} \in \mathbb{R}^{n_{stick} \times (2n_{mas}+2n_{sl})}$ is the assembly of all linearizations of $\mathbf{C}_{t,St}$ with respect to displacements and $\mathbf{P}_{St} \in \mathbb{R}^{n_{s\square ick} \times 2n_{stick}}$ is the

assembly of all linearizations with respect to the Lagrange multipliers (32.c ,64). In the ninth row, $\mathbf{G} \in \mathbb{R}^{n_{slip} \times (2n_{mas}+2n_{sl})}$ is the assembly of all linearizations of $\mathbf{C}_{t,Sl}$ with respect to displacements and $\mathbf{L}_{Sl} \in \mathbb{R}^{n_{slip} \times 2n_{slip}}$ is the assembly of all linearizations with respect to the Lagrange multipliers (36.c ,65).

This system contains both displacement and Lagrange multiplier degrees of freedom. For efficient solution of the system, the Lagrange multipliers are condensed out in the following two stages. First, because the Lagrange multipliers of the inactive nodes are zero, the sixth row and column are eliminated. Second, the diagonality of $\mathbf{D}_S$ enables expressing the Lagrange multipliers of the stick and slip nodes as

$$\begin{aligned} \boldsymbol{\lambda}_{St} &= \mathbf{D}_{SSt}{}^{-1}\left(\mathbf{r}_{St} - \mathbf{K}_{StN}\Delta\mathbf{d}_N - \widetilde{\mathbf{K}}_{StM}\Delta\mathbf{d}_M - \widetilde{\mathbf{K}}_{StI}\Delta\mathbf{d}_I - \widetilde{\mathbf{K}}_{StSt}\Delta\mathbf{d}_{St} - \widetilde{\mathbf{K}}_{StSl}\Delta\mathbf{d}_{Sl}\right) \\ \boldsymbol{\lambda}_{Sl} &= \mathbf{D}_{SSl}{}^{-1}\left(\mathbf{r}_{Sl} - \mathbf{K}_{SlN}\Delta\mathbf{d}_N - \widetilde{\mathbf{K}}_{SlM}\Delta\mathbf{d}_M - \widetilde{\mathbf{K}}_{SlI}\Delta\mathbf{d}_I - \widetilde{\mathbf{K}}_{SlSt}\Delta\mathbf{d}_{St} - \widetilde{\mathbf{K}}_{SlSl}\Delta\mathbf{d}_{Sl}\right) \end{aligned} \tag{50}$$

Substituting into (49), a reduced system with only displacement degrees of freedom is obtained as

$$\begin{bmatrix} \mathbf{K}_{NN} & \mathbf{K}_{NM} & \mathbf{K}_{NI} & \mathbf{K}_{NSt} & \mathbf{K}_{NSl} \\ \begin{pmatrix}\mathbf{K}_{MN} \\ +\widehat{\mathbf{M}}_{MSt}^T\mathbf{K}_{StN} \\ +\widehat{\mathbf{M}}_{MSl}^T\mathbf{K}_{SlN}\end{pmatrix} & \begin{pmatrix}\widetilde{\mathbf{K}}_{MM} \\ +\widehat{\mathbf{M}}_{MSt}^T\widetilde{\mathbf{K}}_{StM} \\ +\widehat{\mathbf{M}}_{MSl}^T\widetilde{\mathbf{K}}_{SlM}\end{pmatrix} & \begin{pmatrix}\widetilde{\mathbf{K}}_{MI} \\ +\widehat{\mathbf{M}}_{MSt}^T\widetilde{\mathbf{K}}_{StI} \\ +\widehat{\mathbf{M}}_{MSl}^T\widetilde{\mathbf{K}}_{SlI}\end{pmatrix} & \begin{pmatrix}\widetilde{\mathbf{K}}_{MSt} \\ +\widehat{\mathbf{M}}_{MSt}^T\widetilde{\mathbf{K}}_{StSt} \\ +\widehat{\mathbf{M}}_{\square Sl}^T\widetilde{\mathbf{K}}_{SlSt}\end{pmatrix} & \begin{pmatrix}\widetilde{\mathbf{K}}_{MSl} \\ +\widehat{\mathbf{M}}_{MSt}^T\widetilde{\mathbf{K}}_{StSl} \\ +\widehat{\mathbf{M}}_{MSl}^T\widetilde{\mathbf{K}}_{SlSl}\end{pmatrix} \\ \mathbf{K}_{IN} & \widetilde{\mathbf{K}}_{IM} & \widetilde{\mathbf{K}}_{II} & \widetilde{\mathbf{K}}_{ISt} & \widetilde{\mathbf{K}}_{ISl} \\ 0 & \mathbf{S}_{AM} & \mathbf{S}_{AI} & \mathbf{S}_{ASt} & \mathbf{S}_{ASl} \\ \mathbf{P}_{St}\mathbf{D}_{SSt}^{-1}\mathbf{K}_{StN} & \begin{pmatrix}\mathbf{P}_{St}\mathbf{D}_{S\square t}^{-1}\widetilde{\mathbf{K}}_{StM} \\ -\mathbf{F}_{StM}\end{pmatrix} & \begin{pmatrix}\mathbf{P}_{St}\mathbf{D}_{SSt}^{-1}\widetilde{\mathbf{K}}_{StI} \\ -\mathbf{F}_{StI}\end{pmatrix} & \begin{pmatrix}\mathbf{P}_{St}\mathbf{D}_{SSt}^{-1}\widetilde{\mathbf{K}}_{StSt} \\ -\mathbf{F}_{StSt}\end{pmatrix} & \begin{pmatrix}\mathbf{P}_{St}\mathbf{D}_{SSt}^{-1}\widetilde{\mathbf{K}}_{StSl} \\ -\mathbf{F}_{StSl}\end{pmatrix} \\ \mathbf{L}_{Sl}\mathbf{D}_{SSl}^{-1}\mathbf{K}_{SlN} & \begin{pmatrix}\mathbf{L}_{Sl}\mathbf{D}_{SSl}^{-1}\widetilde{\mathbf{K}}_{SlM} \\ -\mathbf{G}_{SlM}\end{pmatrix} & \begin{pmatrix}\mathbf{L}_{Sl}\mathbf{D}_{SSl}^{-1}\widetilde{\mathbf{K}}_{SlI} \\ -\mathbf{G}_{SlI}\end{pmatrix} & \begin{pmatrix}\mathbf{L}_{Sl}\mathbf{D}_{SSl}^{-1}\widetilde{\mathbf{K}}_{SlSt} \\ -\mathbf{G}_{SlSt}\end{pmatrix} & \begin{pmatrix}\mathbf{L}_{Sl}\mathbf{D}_{SSl}^{-1}\widetilde{\mathbf{K}}_{SlSl} \\ -\mathbf{G}_{SlSl}\end{pmatrix} \end{bmatrix}$$

$$\begin{bmatrix}\Delta\mathbf{d}_N \\ \Delta\mathbf{d}_M \\ \Delta\mathbf{d}_I \\ \Delta\mathbf{d}_{St} \\ \Delta\mathbf{d}_{Sl}\end{bmatrix} = -\begin{bmatrix} \mathbf{r}_N \\ \mathbf{r}_M + \widehat{\mathbf{M}}_{MSt}^T\mathbf{r}_{St} + \widehat{\mathbf{M}}_{MSl}^T\mathbf{r}_{Sl} \\ \mathbf{r}_I \\ \mathbf{g}_{nA} \\ \mathbf{P}_{St}\mathbf{D}_{SSt}^{-1}\mathbf{r}_{St} - \mathbf{C}_{t,St} \\ \mathbf{L}_{Sl}\mathbf{D}_{SSl}^{-1}\mathbf{r}_{Sl} - \mathbf{C}_{t,Sl} \end{bmatrix}, \tag{51}$$

where $\widehat{\mathbf{M}} = \mathbf{D}^{-1}\mathbf{M}$.

6.4. Primal–dual active set algorithm

Initialize $\mathbf{d}^0$, $\dot{\mathbf{d}}^0 \Longrightarrow \ddot{\mathbf{d}}^0$ and $\mathbf{z}^0$

Loop over all time steps

For a given time step at $t + \alpha$

Set k = 0 and initialize ${}^0\mathbf{d} = \mathbf{d}^t$, ${}^0\boldsymbol{\lambda}^{t+\hat{\alpha}} = \boldsymbol{\lambda}^{(t-1)+\hat{\alpha}}$, ${}^0I = I^t$, ${}^0St = St^t$, ${}^0Sl = Sl^t$, and ${}^0A = {}^0St \cup {}^0Sl$

1. Find $\Delta\,{}^k\mathbf{d}$ and ${}^{k+1}\boldsymbol{\lambda}^{t+\hat{\alpha}}$ by solving

$$\Delta\,{}^k\mathbf{r}^{t+\hat{\alpha}} = -\,{}^k\mathbf{r}^{t+\hat{\alpha}} \tag{52.a}$$

$${}^{k+1}\boldsymbol{\lambda}_j^{t+\hat{\alpha}} = 0, \qquad j \in {}^kI \tag{52.b}$$

$$\Delta\,{}^k\tilde{g}_j^{t+\hat{\alpha}} = -\,{}^k\tilde{g}_j^{t+\hat{\alpha}}, \qquad j \in {}^kA \tag{52.c}$$

$$\Delta\,{}^kC_{tj,St}^{t+\hat{\alpha}} = -\,{}^kC_{tj,St}^{t+\hat{\alpha}}, \qquad j \in {}^kSt \tag{52.d}$$

$$\Delta\,{}^kC_{tj,Sl}^{t+\hat{\alpha}} = -\,{}^kC_{tj,Sl}^{t+\hat{\alpha}}, \qquad j \in {}^kSl \tag{52.e}$$

2. Update ${}^{k+1}\mathbf{d}^{t+1} = {}^k\mathbf{d}^{t+1} + \Delta\,{}^k\mathbf{d}$ and the variables associated with friction laws

3. Update ${}^{k+1}I$, ${}^{k+1}A$, ${}^{k+1}St$, and ${}^{k+1}Sl$ as

$${}^{k+1}I := \left\{j \in |\,{}^{k+1}\lambda_{nj}^{t+\hat{\alpha}} - c_n\,{}^{k+1}\tilde{g}_j^{test} \le 0\right\}$$

$${}^{k+1}A := \left\{j \in |\,{}^{k+1}\lambda_{nj}^{t+\hat{\alpha}} - c_n\,{}^{k+1}\tilde{g}_j^{test} > 0\right\},$$

$${}^{k+1}St := \left\{j \in {}^{k+1}A \middle|\middle| \left({}^{k+1}\lambda_{tj}^{t+\hat{\alpha}} + c_t\,{}^{k+1}\tilde{v}_{tj}^{t+\hat{\alpha}}\right)\right| - {}^{k+1}\mu_j^{t+\hat{\alpha}}\left({}^{k+1}\lambda_{nj}^{t+\hat{\alpha}} - c_n\,{}^{k+1}\tilde{g}_j^{test}\right) < 0\right\}$$

$${}^{k+1}Sl := \left\{j \in {}^{k+1}A \middle|\middle| \left({}^{k+1}\lambda_{tj}^{t+\hat{\alpha}} + c_t\,{}^{k+1}\tilde{v}_{tj}^{t+\hat{\alpha}}\right)\right| - {}^{k+1}\mu_j^{t+\hat{\alpha}}\left({}^{k+1}\lambda_{nj}^{t+\hat{\alpha}} - c_n\,{}^{k+1}\tilde{g}_j^{test}\right) \ge 0\right\}$$

(53)

4. If ${}^{k+1}I = {}^{k}I$, ${}^{k+1}St = {}^{k}St$, ${}^{k+1}Sl = {}^{k}Sl$ and the convergence criterion is satisfied continue to stage 5, else set $k = k + 1$ and go to stage 1
5. Update $\dot{\mathbf{d}}^{t+\Delta t}$ and $\ddot{\mathbf{d}}^{t+\Delta t}$ with the time discretization scheme

7. Examples

In this section, several numerical examples are provided in order to demonstrate the capabilities of the method, examine the accuracy of implementation of the highly non-linear RS friction law, and to evaluate the convergence and energy preservation properties of the method for different time discretization schemes.

7.1. Quasi-static benchmark for rate and state friction

Although this paper mostly focuses on the dynamic response of a contact with variable friction, to verify the implementation of RS friction into the Mortar method, we begin with the following quasi-static numerical test. A 5 x 10 cm rectangular body with a fault at an orientation of 45° and non-matching grid is subjected to the boundary conditions shown in Figure 3a. An elastic material is assumed with Young's modulus E = 40 GPa and Poisson's ratio $\nu = 0.25$. The fault is governed by RS friction with $\mu^* = 0.6$, $v^* = 1 \times 10^{-6}$ m/s, $v_{th} = 10^{-9}$, $a = 0.01$, $b = 0.012$, and $L = 50$ μm. At the beginning the fault is locked, then with increasing slip of the upper edge, and consequently shear stress on the fault, the upper block begins to slide relative to the lower block and shortly approaches a steady state constant sliding velocity of $v = 1 \times 10^{-6}$ m/s. At this stage we increase the velocity of the upper edge by a factor of 10 and examine the response of the friction coefficient on the central node of the upper side of the fault (Figure 3b). Because the relative slip rate on the fault does not increase immediately by a factor of 10 as on the

boundary, the peak value of the numerical friction coefficient is slightly lower than that of the analytic, but after two time steps the numerical solution converges to the analytic solution quite well.

7.2. Dynamic rupture with slip-weakening friction

In this section, we demonstrate the effectiveness of the method in studying dynamic shear rupture problems on rough faults governed by SW friction. We consider a two dimensional plane strain model of a 20 m self-affine rough fault embedded in a 60 x 30 m elastic domain subjected to a simple shear loading conditions. The mechanical properties of the domain and the loading conditions are shown in Figure 4a. This setup results in a gradual increase of the shear load on the fault, thus the nucleation of the rupture is completely spontaneous. The geometry of the fault is shown in Figure 4b and the fault is governed by the following SW parameters: $\mu_s = 0.6$, $\mu_d = 0.55$, and $D_c = 0.3$ mm. In order to represent properly the chosen minimum wavelength of roughness (20 cm) with the mesh, we use hanging nodes to gradually refine the quadrilateral element from a size of about 1 x 1 m near the boundaries of the model to about 1.56 x 1.56 cm around the fault. This leads to 1281 nodes on each side of the fault. We perform four simulations with different values of the time scheme parameters in (23) as follows: (1) Midpoint scheme ($\alpha = 0.5$, $\beta = 0.5$, and $\gamma = 1$); (2) average acceleration Newmark scheme ($\alpha = 1$, $\beta = 0.25$, and $\gamma = 0.5$); (3) Newmark scheme with a small damping ($\alpha = 1$, $\beta = 0.3$, and $\gamma = 0.6$); and (4) Newmark scheme with a larger damping ($\alpha = 1$, $\beta = 0.5$, and $\gamma = 1$). In order to load the fault, all simulations begin with several large quasi-static time steps, then the time step size is reduced to $\Delta t = 20\ \mu s$ and the simulations continue dynamically.

Figure 5 shows snapshots of the distribution of shear stress around the fault at four different stages of the rupture for a simulation with time discretization scheme #3. The first stage corresponds to the end of the quasi-static loading stage. At this stage, a few small regions with preferable local orientation of the fault begin to slip with a small decrease in the friction coefficient and shear stress. At the second stage, a 2m long rupture nucleates from one of these regions with further decreases in shear stress and development of stress concentrations at its tips. At the third stage, the rupture expands at velocities of about 2200 m/s and 2400 m/s to the left and right sides, respectively. Finally, the entire fault ruptures and slips, and large shear stresses are observed at the tips, as well as significant variations in shear stress with the local geometry of the fault.

To study the effects of the time discretization parameters, we examine the evolution of sliding velocity and shear traction with time in all simulations at the two nodes on the fault shown in Figure 5. The locations are chosen to represent both the nucleation (node *A*) and propagation (node *B*) phases of the rupture. As expected, the latter shows a narrower velocity curve with a larger peak (Figures 6a and 6b), which slightly decreases with increasing damping in the time discretization schemes. In both locations, the general behavior of the velocity curve is similar for all of the time discretization schemes we tested, where the differences between schemes #1 and #2 are negligible and the other schemes damp mostly the high frequency content of the curve. The shear traction at node *A* decreases from its initial value to its residual value over about 3 ms (Figure 6c), while, at node *B*, the shear traction initially increases over about 0.5 ms and then decreases sharply to a residual value (Figure 6d). In both locations, there is a further moderate decrease in shear traction, followed by larger variations resulting

from the arrest of the rupture at the tips of the fault. Differences among the time schemes are observed mostly at this last stage.

Next, we examine the effects of the time discretization schemes on the energy components in the system for the problem described above. A scheme conserves energy if at a given time step

$$\mathbf{E}_{pot}^{t+1} + \mathbf{E}_{kin}^{t+1} - (\mathbf{E}_{ext}^{t+1} - \mathbf{E}_{con}^{t+1}) = 0, \tag{54}$$

where the potential energy is given by

$$\mathbf{E}_{pot}^{t+1} = \mathbf{E}_{pot}^{t} + 0.5\boldsymbol{\Delta}\mathbf{d}^{T}(\mathbf{f}_{int}^{t} + \mathbf{f}_{int}^{t+1}), \tag{55}$$

the kinetic energy is given by

$$\mathbf{E}_{kin}^{t+1} = 0.5\dot{\mathbf{d}}^{t+1^{T}}\mathbf{M}\dot{\mathbf{d}}^{t+1} \tag{56}$$

the contact work is given by

$$\mathbf{E}_{c}^{t+1} = \begin{cases} \mathbf{E}_{c}^{t} + 0.5\boldsymbol{\Delta}\mathbf{d}^{T}(\mathbf{f}_{c}^{t} + \mathbf{f}_{c}^{t+1}), & \alpha = 1 \\ \mathbf{E}_{c}^{t} + \boldsymbol{\Delta}\mathbf{d}^{T}\left(\mathbf{f}_{c}^{t+\hat{\alpha}}\right), & \alpha = 1/2 \end{cases}, \tag{57}$$

and the external work is given by

$$\mathbf{E}_{ext}^{t+1} = \mathbf{E}_{ext}^{t} + 0.5\boldsymbol{\Delta}\mathbf{d}^{T}(\mathbf{f}_{ext}^{t} + \mathbf{f}_{ext}^{t+1}). \tag{58}$$

As expected, schemes #3 and #4, which involve algorithmic damping, slightly dissipate energy with a smaller decrease of the potential energy and correspondingly a smaller increase of the contact work and kinetic energy with time compared to schemes #1 and #2 (Figure 7). However, it is important to note that this effect decreases with decreasing time step size and vice versa. While scheme #2 exactly conserves energy, a slight growth in the total energy is observed for scheme #1.

To examine the convergence behavior of the method, Figure 8 shows the number of iterations and number of slipping nodes during the simulation for schemes #1 and #4.

Both schemes show excellent convergence despite the large number of nodes on the fault. Scheme #1 shows more changes between slipping and sticking nodes and consequently slightly more iterations. Between time step 250 and time step 800, when most of the rupture process occurs, the average number of iterations per time step of scheme #1 is 3.9, while that of scheme #4 is 3.2. Schemes #2 and #3 show similar behavior with average numbers of iterations of 3.7 and 3.25, respectively.

7.3. Rupture with rate and state friction

Using the same problem setup as in Figure 4a, we demonstrate the capability of the method to study physical problems that involve frictional instability on a rougher fault governed by RS friction. We use the same RS friction parameters as in section 7.1 and increase the roughness amplitude by a factor of two. In order to model the evolution of the friction coefficient accurately during the nucleation and propagation phases of the rupture, the time step varies such that the maximum relative slip in a given time step is smaller than half of the critical slip distance L. This leads to a significant reduction in time step size from a value of Δt = 1000 s to Δt = 10 μs during the nucleation phase and additional decrease to a value of Δt = 3 μs during the propagation phase. To examine the energy conservation property also at the stage of the rupture arrest, we do not allow the time step size to increase back, and fix it at a value of Δt = 10 μs. The transition from quasi-static to dynamic time integration is performed when the time step size decreases below 0.001 s.

Figure 9a shows the time evolution of slip along the fault for a simulation with time discretization scheme #2. The initial quasi-static stage is represented by red contours at decreasing time intervals, while the dynamic stage is represented by black contours at

the time interval set to a value of $5x10^{-4}$ s. At the end of the quasi-static stage most of the slip occurs along a portion of the fault between 10.5 and 14 m. With the transition to the dynamic stages we observe a complex behavior of the rupture, with asymmetric expansion of rupture and large spatial variations of the final slip that correspond to the local geometry of the fault. Moreover, the rupture velocity V_r varies significantly with the local geometry of the fault (Figure 9b).

Similar to section 7.2, we examine the effect of the time discretization schemes on the evolution of sliding velocity and shear traction at nodes *A* and *B*. Although the sliding velocity is generally larger than that obtained with SW, the difference between the time discretization schemes is smaller (Figures 10a and 10b) and is observed mostly at the stage where the rupture decelerates. In general, the combination of larger roughness together with RS friction results in a complex behavior of the shear traction with large temporal variations, including an initial strengthening stage also at node *A* and very high traction concentrations at node *B* (Figures 10c and 10d). In both locations, the final stage of the simulations with no damping involves large oscillations in the shear traction. It is important to note that these oscillations are not the result of numerical errors, but are the result of the propagation of waves in the domain and the arrest of the rupture at the tips of the fault.

Figure 11 shows the energy partitioning during the rupture process. The initial stage of strengthening in the RS friction law leads to a larger potential energy compared to the case of the SW friction law and consequently the kinetic energy and contact work components are larger. During the propagation phase of the rupture the energy dissipation in damping schemes (#3 and #4) is quite small because of the small time step size. An

increase in energy dissipation is observed during the arrest of the rupture, where the time step size is larger. Similar to the case of the SW friction law, scheme #2 exactly conserves energy and a slight growth in the total energy is observed for scheme #1.

To study the convergence behavior of the method, Figure 12 shows the number of iterations and number of slipping and inactive nodes during the simulation for schemes #1 and #4. In general good convergence is observed, although the high nonlinearity of the RS friction law and the larger roughness amplitude result in slower convergence rate compared to the previous example. Moreover, small portions of the fault open near the end of the simulations and 30 nodes become inactive. The algorithmic damping improves the convergence rate, with an average number of iterations per time step of 6.4 for scheme #4 and 7.4 for scheme #1. Scheme #4 also shows a more steady convergence rate. Schemes #2 and #3 show similar behavior with an average number of iterations of 8.3 and 7, respectively. All schemes show smaller convergence rates near the end of the simulation. At this stage the slip rate along the fault is small (see Figure 10), but with the RS friction law small changes in the slip rate result in large variations in the friction coefficient. These variations, together with variations in the normal and shear tractions on the fault because of propagating elastic waves in the medium, result in a slower convergence rate.

8. Conclusions

We extend the 2D finite deformation mortar formulation to dynamic problems and implement SW and RS friction laws into the method. We utilize the dual Lagrange multipliers and the primal–dual active set strategy concepts and accordingly discretize and linearize the friction laws to obtain a semi-smooth Newton method. Moreover, the

discretization of the RS friction law involves a procedure to condense out the state variables, thus eliminating the addition of another set of unknowns into the system.

Several numerical examples are provided in order to demonstrate the capabilities of the method for modeling shear rupture on rough surfaces governed by SW and RS friction laws. The effect of the different time discretization schemes on the convergence, energy conservation, and the time evolution of shear traction and slip rate is examined. The method shows excellent convergence for the SW friction law with efficient detection between the slipping and sticking states of the nodes despite the large number of nodes on the fault. A good convergence is also obtained for the RS friction law, but because of its high nonlinearity and because it involves significant variations of the friction coefficient with small change in slip rate, more iterations are needed before convergence. For both friction laws, the total energy is exactly conserved with the non-damping Newmark scheme and experiences very small growth with the mid-point scheme. The amount of energy dissipation in the damping schemes is quite small. It decreases with decreasing time step size and affects mostly the very high frequency variations in the shear traction and slip rate.

Acknowledgements

This work was supported by Aramco grant 6500009957 and the Southern California Earthquake Center (SCEC) grant 16108. SCEC is funded by NSF Cooperative Agreement EAR-1033462 and USGS Cooperative Agreement G12AC20038.

Appendix A: The mortar integral matrices

The coupling matrices $\mathbf{D}_S$ and $\mathbf{M}_M$ arising from the mortar integrals are evaluated as

$$\mathbf{D}_S[j,j] = D_{jj}\mathbf{I} = \int_{\gamma_c^{(1)}} N_j^{(1)} d\gamma\, \mathbf{I}, \quad j = 1, \dots, n_{sl} \tag{59}$$

$$\mathbf{M}_M[j,l] = M_{jl}\mathbf{I} = \int_{\gamma_c^{(1)}} \phi_j N_l^{(2)} d\gamma\, \mathbf{I}, \quad j = 1, \dots, n_{sl}\,, \quad l = 1, \dots, n_{mas} \tag{60}$$

While numerical integration of the mortar matrix $\mathbf{D}_S$ involves simply the integration of the slave side displacement shape functions over the current slave contact, numerical integration of the mortar matrix $\mathbf{M}_M$ is more complex because it involves the product of master side shape functions and slave side dual shape functions over the slave contact surface. To perform this integration, we follow the approach in [17, 27], in which the integration domain is discretized into contact segments, on which both shape functions are defined continuously.

Appendix B: Linearization details

An important aspect of section 6.2 is the consistent linearization of (32). We supply linearization details in this section of the appendix.

The linearization of the force equilibrium in (32.a) is given by

$$\begin{aligned} \Delta\, {}^{k}\mathbf{r}^{t+\hat{\alpha}} &= \Delta\left(\frac{1}{\beta\Delta t^2}\mathbf{M}\, {}^{k}\mathbf{d}^{t+\Delta t} + \mathbf{f}_{int}\left({}^{k}\mathbf{d}^{t+\alpha}\right) + \mathbf{f}_c\left({}^{k}\mathbf{d}^{t+\alpha},\, {}^{k}\boldsymbol{\lambda}^{t+\hat{\alpha}}\right)\right) \\ &= \left(\frac{1}{\beta\Delta t^2}\mathbf{M} + {}^{k}\mathbf{K}_{int}^{t+\hat{\alpha}}\right)\Delta\mathbf{d} + \Delta\, {}^{k}\mathbf{f}_c^{t+\hat{\alpha}} = {}^{k}\mathbf{K}^{t+\hat{\alpha}}\Delta\mathbf{d} + \Delta\, {}^{k}\mathbf{f}_c^{t+\hat{\alpha}} \\ &= \mathbf{f}_{ext}^{t+\alpha} + \mathbf{R} - \frac{1}{\beta\Delta t^2}\mathbf{M}\, {}^{k}\mathbf{d}^{t+\Delta t} - {}^{k}\mathbf{f}_{int}^{t+\hat{\alpha}} - {}^{k}\mathbf{f}_c^{t+\hat{\alpha}} = -\,{}^{k}\mathbf{r}^{t+\hat{\alpha}} \end{aligned} \tag{61}$$

where ${}^{k}\mathbf{K}_{int}^{t+\hat{\alpha}}$ is the tangent stiffness matrix and ${}^{k}\mathbf{K}^{t+\hat{\alpha}}$ is an effective stiffness matrix defined as ${}^{k}\mathbf{K}^{t+\hat{\alpha}} = \left(\frac{1}{\beta\Delta t^2}\mathbf{M} + {}^{k}\mathbf{K}_{int}^{t+\hat{\alpha}}\right)$. The linearization of the contact forces can be expressed as

$$
\begin{aligned}
\Delta\, {}^{k}\mathbf{f}_c^{t+\hat{\alpha}} &= \left[\mathbf{0}, \Delta\left(-\,{}^{k}\mathbf{M}_M^{t+\alpha^T}\,{}^{k}\boldsymbol{\lambda}^{t+\hat{\alpha}}\right), \Delta\left(\,{}^{k}\mathbf{D}_S^{t+\alpha^T}\,{}^{k}\boldsymbol{\lambda}^{t+\hat{\alpha}}\right)\right] \\
&= \left[\mathbf{0}, \Delta\left(-\alpha\,{}^{k}\mathbf{M}_M^{t+1^T}\right)\,{}^{k}\boldsymbol{\lambda}^{t+\hat{\alpha}}, \Delta\left(\alpha\,{}^{k}\mathbf{D}_S^{t+1^T}\right)\,{}^{k}\boldsymbol{\lambda}^{t+\hat{\alpha}}\right] \\
&\quad + \left[\mathbf{0}, -\,{}^{k}\mathbf{M}_M{}^{T},\ {}^{k}\mathbf{D}_S{}^{T}\right]\Delta\,{}^{k}\boldsymbol{\lambda}^{t+\hat{\alpha}} \qquad (62) \\
&\coloneqq \alpha\,{}^{k}\tilde{\mathbf{C}}\Delta\,{}^{k}\mathbf{d}_{SM} + \left[\mathbf{0}, -\,{}^{k}\mathbf{M}_M^{t+\alpha^T},\ {}^{k}\mathbf{D}_S^{t+\alpha^T}\right]\left({}^{k+1}\boldsymbol{\lambda}^{t+\hat{\alpha}} - \,{}^{k}\boldsymbol{\lambda}^{t+\hat{\alpha}}\right) \\
&= -\left[\mathbf{0}, -\,{}^{k}\mathbf{M}_M^{t+\alpha^T},\ {}^{k}\mathbf{D}_S^{t+\alpha^T}\right]\,{}^{k}\boldsymbol{\lambda}^{t+\hat{\alpha}} = -\,{}^{k}\mathbf{f}_c^{t+\hat{\alpha}}
\end{aligned}
$$

where the matrix $\tilde{\mathbf{C}} \in \mathbb{R}^{(2n_{sl}+2n_{mas})\times(2n_{sl}+2n_{mas})}$ includes the directional derivatives of mortar matrices $\mathbf{M}_M$ and $\mathbf{D}_S$ multiplied by the current Lagrange multiplier values ${}^{k}\boldsymbol{\lambda}^{t+\hat{\alpha}}$ and $\Delta\,{}^{k}\mathbf{d}_{SM} \in \mathbb{R}^{2n_{sl}+2n_{mas}}$ are the corresponding incremental displacements of slave (*S*) and master (*M*) nodes. The directional derivatives of mortar matrices $\mathbf{M}_M$ and $\mathbf{D}_S$ are given in [27].

The linearization of the contact condition in the normal direction (32.b) involves the directional derivative of the gap function (35.b), which is given by

$$
\begin{aligned}
\Delta\,{}^{k}\dot{\tilde{g}}_{nj}^{t+\hat{\alpha}} &= -\,{}^{k}\mathbf{n}_j^{t+\alpha^T}\left(\,{}^{k}\mathbf{D}_S^{t+\alpha}[j,j]\Delta\,{}^{k}\dot{\mathbf{d}}_j^{t+\alpha} - \sum_{l=1}^{n_{mas}}\,{}^{k}\mathbf{M}_M^{t+\alpha}[j,l]\Delta\,{}^{k}\dot{\mathbf{d}}_l^{t+\alpha}\right) \\
&\quad - \alpha\Delta\,{}^{k}\mathbf{n}_j^{t+1^T}\left(\,{}^{k}\mathbf{D}_S^{t+\alpha}[j,j]\,{}^{k}\dot{\mathbf{d}}_j^{t+\alpha} - \sum_{l=1}^{n_{mas}}\,{}^{k}\mathbf{M}_M^{t+\alpha}[j,l]\,{}^{k}\dot{\mathbf{d}}_l^{t+\alpha}\right) \qquad (63) \\
&\quad - \,{}^{k}\mathbf{n}_j^{t+\alpha^T}\left(\alpha\Delta\,{}^{k}\mathbf{D}_S^{t+1}[j,j]\,{}^{k}\dot{\mathbf{d}}_j^{t+\alpha} - \sum_{l=1}^{n_{mas}}\alpha\Delta\,{}^{k}\mathbf{M}_M^{t+1}[j,l]\,{}^{k}\dot{\mathbf{d}}_l^{t+\alpha}\right),
\end{aligned}
$$

where $\Delta\,{}^{k}\dot{\mathbf{d}}^{t+\alpha} = \frac{\alpha\gamma}{\beta\Delta t}\Delta\,{}^{k}\mathbf{d}^{t+1}$ and the directional derivative of the unit normal vector ${}^{k}\mathbf{n}_j^{t+1}$ is given in [27].

In the tangential direction, the directional derivatives of the contact condition (32.c) with a variable friction coefficient becomes

$$\begin{aligned}\Delta\,{}^{k}C_{tj,St}^{t+\hat{\alpha}} = &-{}^{k}\mu_j^{t+\hat{\alpha}}\left({}^{k}\lambda_{nj}^{t+\hat{\alpha}} - c_n\,{}^{k}\dot{\tilde{g}}_{nj}^{t+\hat{\alpha}}\right)c_t\Delta\,{}^{k}\tilde{v}_{tj}^{t+\hat{\alpha}}\\ &-{}^{k}\mu_j^{t+\hat{\alpha}}\left(\Delta\,{}^{k}\lambda_{nj}^{t+\hat{\alpha}} - c_n\Delta\,{}^{k}\dot{\tilde{g}}_{nj}^{t+\hat{\alpha}}\right)c_t\,{}^{k}\tilde{v}_{tj}^{t+\hat{\alpha}}\\ &-\Delta\,{}^{k}\mu_j^{t+\hat{\alpha}}\left({}^{k}\lambda_{nj}^{t+\hat{\alpha}} - c_n\,{}^{k}\dot{\tilde{g}}_{nj}^{t+\hat{\alpha}}\right)c_t\,{}^{k}\tilde{v}_{tj}^{t+\hat{\alpha}}\\ = &\;{}^{k}\mu_j^{t+\hat{\alpha}}\left({}^{k}\lambda_{nj}^{t+\hat{\alpha}} - c_n\,{}^{k}\dot{\tilde{g}}_{nj}^{t+\hat{\alpha}}\right)c_t\,{}^{k}\tilde{v}_{tj}^{t+\hat{\alpha}} = -\,{}^{k}C_{tj,St}^{t+\hat{\alpha}}, \qquad j\in\,{}^{k}St\end{aligned} \tag{64}$$

and

$$\begin{aligned}\Delta\,{}^{k}C_{tj,Sl}^{t+\hat{\alpha}} = &\left|\,{}^{k}\lambda_{tj}^{t+\hat{\alpha}} + c_t\,{}^{k}\tilde{v}_{tj}^{t+\hat{\alpha}}\right|\Delta\,{}^{k}\lambda_{tj}^{t+\hat{\alpha}}\\ &+\frac{\left({}^{k}\lambda_{tj}^{t+\hat{\alpha}} + c_t\,{}^{k}\tilde{v}_{tj}^{t+\hat{\alpha}}\right)}{\left|\,{}^{k}\lambda_{tj}^{t+\hat{\alpha}} + c_t\,{}^{k}\tilde{v}_{tj}^{t+\hat{\alpha}}\right|}\,{}^{k}\lambda_{tj}^{t+\hat{\alpha}}\left(\Delta\,{}^{k}\lambda_{tj}^{t+\hat{\alpha}} + c_t\Delta\,{}^{k}\tilde{v}_{tj}^{t+\hat{\alpha}}\right)\\ &-{}^{k}\mu_j^{t+\hat{\alpha}}\left({}^{k}\lambda_{nj}^{t+\hat{\alpha}} - c_n\,{}^{k}\dot{\tilde{g}}_{nj}^{t+\hat{\alpha}}\right)\left(\Delta\,{}^{k}\lambda_{tj}^{t+\hat{\alpha}} + c_t\Delta\,{}^{k}\tilde{v}_{tj}^{t+\hat{\alpha}}\right)\\ &-{}^{k}\mu_j^{t+\hat{\alpha}}\left(\Delta\,{}^{k}\lambda_{nj}^{t+\hat{\alpha}} - c_n\Delta\,{}^{k}\dot{\tilde{g}}_{nj}^{t+\hat{\alpha}}\right)\left({}^{k}\lambda_{tj}^{t+\hat{\alpha}} + c_t\,{}^{k}\tilde{v}_{tj}^{t+\hat{\alpha}}\right)\\ &-\Delta\,{}^{k}\mu_j^{t+\hat{\alpha}}\left({}^{k}\lambda_{nj}^{t+\hat{\alpha}} - c_n\,{}^{k}\dot{\tilde{g}}_{nj}^{t+\hat{\alpha}}\right)\left({}^{k}\lambda_{tj}^{t+\hat{\alpha}} + c_t\,{}^{k}\tilde{v}_{tj}^{t+\hat{\alpha}}\right)\\ = -\left|\,{}^{k}\lambda_{tj}^{t+\hat{\alpha}} + c_t\,{}^{k}\tilde{v}_{tj}^{t+\hat{\alpha}}\right|\,{}^{k}\lambda_{tj}^{t+\hat{\alpha}} + &\;{}^{k}\mu_j^{t+\hat{\alpha}}\left({}^{k}\lambda_{nj}^{t+\hat{\alpha}} - c_n\,{}^{k}\dot{\tilde{g}}_{nj}^{t+\hat{\alpha}}\right)\left({}^{k}\lambda_{tj}^{t+\hat{\alpha}} + c_t\,{}^{k}\tilde{v}_{tj}^{t+\hat{\alpha}}\right)\\ = &-\,{}^{k}C_{tj,Sl}^{t+\hat{\alpha}}, \qquad j\in\,{}^{k}Sl,\end{aligned} \tag{65}$$

for the sticking and slipping nodes, respectively, where the directional derivative of the weighted tangential relative velocity ${}^{k}\tilde{v}_{tj}^{t+\hat{\alpha}}$ is similar to (63) but with ${}^{k}\mathbf{t}_j^{t+\alpha}$ replacing $-\,{}^{k}\mathbf{n}_j^{t+\alpha}$ and $\Delta\,{}^{k}\mathbf{t}_j^{t+\alpha} = \mathbf{e}_3\times\Delta\,{}^{k}\mathbf{n}_j^{t+\alpha}$. The directional derivatives of the normal and tangential components of the Lagrange multiplier are given by

$$\Delta\,{}^{k}\lambda_{nj}^{t+\hat{\alpha}} = \Delta\,{}^{k}\mathbf{n}_j^{t+\alpha}\cdot\,{}^{k}\boldsymbol{\lambda}_j^{t+\hat{\alpha}} + {}^{k}\mathbf{n}_j^{t+\alpha}\cdot\Delta\,{}^{k}\boldsymbol{\lambda}_j^{t+\hat{\alpha}}, \tag{66.a}$$

$$\Delta\,{}^{k}\lambda_{tj}^{t+\hat{\alpha}} = \Delta\,{}^{k}\mathbf{t}_j^{t+\alpha}\cdot\,{}^{k}\boldsymbol{\lambda}_j^{t+\hat{\alpha}} + {}^{k}\mathbf{t}_j^{t+\alpha}\cdot\Delta\,{}^{k}\boldsymbol{\lambda}_j^{t+\hat{\alpha}}, \tag{66.b}$$

where $\Delta\,{}^{k}\boldsymbol{\lambda}_j^{t+\hat{\alpha}} = {}^{k+1}\boldsymbol{\lambda}_j^{t+\hat{\alpha}} - {}^{k}\boldsymbol{\lambda}_j^{t+\hat{\alpha}}$.

References

1. Scholz CH (2002) “The Mechanics of Earthquakes and Faulting - Second Edition”

by Christopher H. Scholz. doi: 10.1785/gssrl.74.3.333

2. Bizzarri A, Cocco M, Andrews DJ, Boschi E (2001) Solving the dynamic rupture problem with different numerical approaches and constitutive laws. Geophys J Int 144:656–678. doi: 10.1046/j.1365-246X.2001.01363.x
3. Klinger Y (2010) Relation between continental strike-slip earthquake segmentation and thickness of the crust. J Geophys Res Solid Earth 115:1–19. doi: 10.1029/2009JB006550
4. Candela T, Renard F, Klinger Y, et al (2012) Roughness of fault surfaces over nine decades of length scales. J Geophys Res Solid Earth 117:1–30. doi: 10.1029/2011JB009041
5. Brown SR, Scholz CH (1985) Broad bandwidth study of the topography of natural rock surfaces. J Geophys Res 90:12575. doi: 10.1029/JB090iB14p12575
6. Power WL, Tullis TE, Brown SR, et al (1987) Roughness of natural fault surfaces. Geophys Res Lett 14:29. doi: 10.1029/GL014i001p00029
7. Power WL, Tullis TE (1991) Euclidean and fractal models for the description of rock surface roughness. J Geophys Res 96:415. doi: 10.1029/90JB02107
8. Renard F, Voisin C, Marsan D, Schmittbuhl J (2006) High resolution 3D laser scanner measurements of a strike-slip fault quantify its morphological anisotropy at all scales. Geophys Res Lett 33:33–36. doi: 10.1029/2005GL025038
9. Sagy A, Brodsky EE, Axen GJ (2007) Evolution of fault-surface roughness with slip. Geology 35:283–286. doi: 10.1130/G23235A.1
10. Candela T, Renard F, Bouchon M, et al (2009) Characterization of fault roughness at various scales: Implications of three-dimensional high resolution topography

measurements. Pure Appl Geophys 166:1817–1851. doi: 10.1007/s00024-009-0521-2

11. Bistacchi A, Ashley Griffith W, Smith SAF, et al (2011) Fault Roughness at Seismogenic Depths from LIDAR and Photogrammetric Analysis. Pure Appl Geophys 168:2345–2363. doi: 10.1007/s00024-011-0301-7
12. Dunham EM, Belanger D, Cong L, Kozdon JE (2011) Earthquake ruptures with strongly rate-weakening friction and off-fault plasticity, part 2: Nonplanar faults. Bull Seismol Soc Am 101:2308–2322. doi: 10.1785/0120100076
13. Fang Z, Dunham EM (2013) Additional shear resistance from fault roughness and stress levels on geometrically complex faults. J Geophys Res Solid Earth 118:3642–3654. doi: 10.1002/jgrb.50262
14. Shi Z, Day SM (2013) Rupture dynamics and ground motion from 3-D rough-fault simulations. J Geophys Res Solid Earth 118:1122–1141. doi: 10.1002/jgrb.50094
15. Bruhat L, Fang Z, Dunham EM (2016) Rupture complexity and the supershear transition on rough faults. J Geophys Res Solid Earth 1–15. doi: 10.1002/2015JB012512.Received
16. Papadopoulos P, Taylor RL (1992) A mixed formulation for the finite element solution of contact problems. Comput Methods Appl Mech Eng 94:373–389.
17. Yang B, Laursen TA, Meng X (2005) Two dimensional mortar contact methods for large deformation frictional sliding. Int J Numer Methods Eng 62:1183–1225. doi: 10.1002/nme.1222
18. Bernardi C, Maday Y, Patera a T (1993) Domain Decomposition by the Mortar Element Method. Asymptot Numer Methods Partial Differ Equations with Crit

Parameters 269–286. doi: 10.1007/978-94-011-1810-1_17

19. Puso MA, Laursen TA (2004) A mortar segment-to-segment frictional contact method for large deformations q. Int J Numer Methods Eng 193:4891–4913. doi: 10.1016/j.cma.2004.06.001

20. Puso MA, Laursen TA, Solberg J (2008) A segment-to-segment mortar contact method for quadratic elements and large deformations. Comput Methods Appl Mech Eng 197:555–566. doi: 10.1016/j.cma.2007.08.009

21. Fischer KA, Wriggers P (2005) Frictionless 2D Contact formulations for finite deformations based on the mortar method. Comput Mech 226–244. doi: 10.1007/s00466-005-0660-y

22. Fischer KA, Wriggers P (2006) Mortar based frictional contact formulation for higher order interpolations using the moving friction cone. Comput Methods Appl Mech Eng 195:5020–5036. doi: 10.1016/j.cma.2005.09.025

23. Wohlmuth BI (2000) A mortar finite element method using dual spaces for the Lagrange multiplier. SIAM J Num Anal 38:989–1012.

24. Hüeber S, Wohlmuth BI (2005) A primal – dual active set strategy for non-linear multibody contact problems q. Comput Methods Appl Mech Eng 194:3147–3166. doi: 10.1016/j.cma.2004.08.006

25. Hüeber S, Stadler G, Wohlmuth BI (2008) A primal–dual active set algorithm for three-dimensional contact problems with Coulomb friction. SIAM J Sci Comput 30:572–596.

26. Brunssen S, Schmid F, Schafer M, Wohlmuth BI (2007) A fast and robust iterative solver for nonlinear contact problems using a primal-dual active set strategy and

algebraic multigrid. Int J Numer Methods Eng 524–543. doi: 10.1002/nme

27. Popp A, Gee MW, Wall WA (2009) A finite deformation mortar contact formulation using a primal–dual active set strategy. Int J Numer Methods Eng 79:1354–1391. doi: 10.1002/nme.2614
28. Gitterle M, Popp A, Gee MW, Wall WA (2010) Finite deformation frictional mortar contact using a semi-smooth Newton method with consistent linearization. Int J Numer Methods Eng 84:543–571. doi: 10.1002/nme.2907
29. Hager C, Hüeber S, Wohlmuth BI (2008) A stable energy-conserving approach for frictional contact problems based on quadrature formulas. Int J Numer Methods Eng 73:205–225.
30. Hager C, Wohlmuth BI (2009) Analysis of a space-time discretization for dynamic elasticity problems based on mass-free surface elements. SIAM J Numer Anal 47:1863–1885.
31. Xu S, Ben-Zion Y, Ampuero J-P, Lyakhovsky V (2015) Dynamic Ruptures on a Frictional Interface with Off-Fault Brittle Damage : Feedback Mechanisms and Effects on Slip and Near-Fault Motion. Pure Appl Geophys 172:1243–1267. doi: 10.1007/s00024-014-0923-7
32. Ida Y (1972) Cohesive force across the tip of a longitudinal-shear crack and Griffith's specific surface energy. J Geophys Res 77:3796. doi: 10.1029/JB077i020p03796
33. Palmer AC, Rice JR (1973) The growth of slip surfaces in the progressive failure of over-consolidated clay. Proc R Soc London A 332:527–548. doi: 10.1098/rspa.1983.0054

34. Andrews DJ (1976) Rupture velocity of plane strain shear cracks. J Geophys Res 81:5679. doi: 10.1029/JB081i032p05679

35. Ohnaka M, Yamashita T (1989) A cohesive zone model for dynamic shear faulting based on experimentally inferred constitutive relation and strong motion source parameters. J Geophys Res 94:4089. doi: 10.1029/JB094iB04p04089

36. Di Toro G, Han R, Hirose T, et al (2011) Fault lubrication during earthquakes. Nature 471:494–498. doi: 10.1038/nature09838

37. Dieterich JH (1979) Modeling of rock friction: 1. Experimental results and constituve equations. J Geophys Res 84:2161–2168. doi: 10.1007/BF00876539

38. Ruina A (1983) Slip instability and state variable friction law. J Geophys Res 88:10359–10370. doi: 10.1029/JB088iB12p10359

39. Beeler NM, Tullis TE, Weeks JD (1994) The roles of time and displacement in the evolution effect in rock friction. Geophys Res Lett 21:1987. doi: 10.1029/94GL01599

40. Bathe KJ (1996) Finite element procedures. Prentice Hall, Upper Saddle River, New Jersey

41. Hartmann S, Brunssen S, Ramm E, Wohlmuth B (2007) Non-Linear Dynamic Problems Using Dual Lagrange Multipliers. 2007:1–4.

42. Hilber HM, Hughes TJR, Taylor RL (1977) Improved numerical dissipation for time integration algorithms in structural dynamics. Earthq Eng Struct Dyn 5:283–292. doi: 10.1002/eqe.4290050306

43. Newmark NM (1959) A method of computation for structural dynamics. J Eng Mech Div 85:67–94.

44. Gonzalez O (2000) Exact energy-momentum conserving algorithms for general models in nonlinear elasticity. Comput Meth Appl Mech 190:1763–1783. doi: 10.1.1.56.3444

45. Laursen TA, Meng XN (2001) A new solution procedures for application of energy-conserving algorithms to general constitutive models in nonlinear elastodynamics. Comput Methods Appl Mech Eng 190:6309–6322. doi: 10.1016/S0045-7825(01)00257-2

46. Laursen T., Chawla V (1997) Design of Energy Conserving Algorithms for Frictionless Dynamic Contact Problems. Int J Numer Methods Eng 40:863–886. doi: 10.1002/(SICI)1097-0207(19970315)40:5<863::AID-NME92>3.0.CO;2-V

47. Hauret P, Tallec P Le (2006) Energy-controlling time integration methods for nonlinear elastodynamics and low-velocity impact. Comput Methods Appl Mech Eng 195:4890–4916. doi: 10.1016/j.cma.2005.11.005

48. Hesch C, Betsch P (2011) Transient three-dimensional contact problems : mortar method . Mixed methods and conserving integration. Comput Mech 48:461–475. doi: 10.1007/s00466-011-0583-8

49. Liu F, Borja RI (2009) An extended finite element framework for slow-rate frictional faulting with bulk plasticity and variable friction. Int J Numer Anal Methods Geomech 33:1535–1560. doi: 10.1002/nag.777

Figures

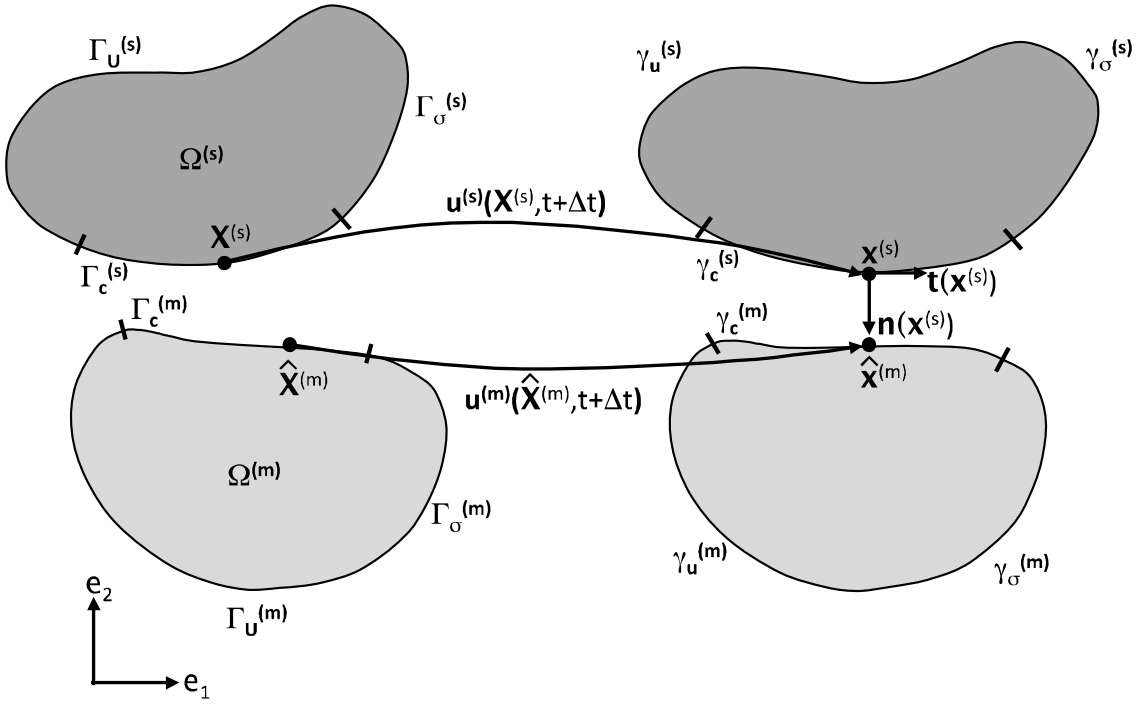

Figure 1. Notation for finite deformation contact problem.

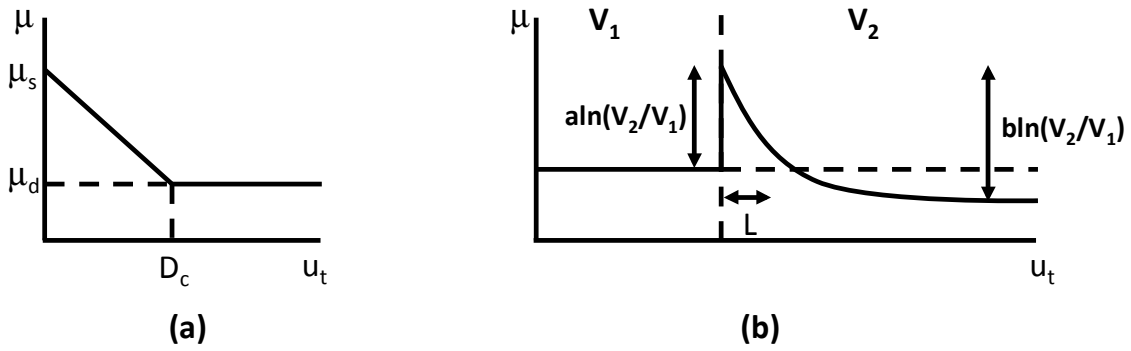

Figure 2. (a) A linear SW friction law. (b) The change in friction in response to sudden increase in sliding velocity as predicted by the RS friction law.

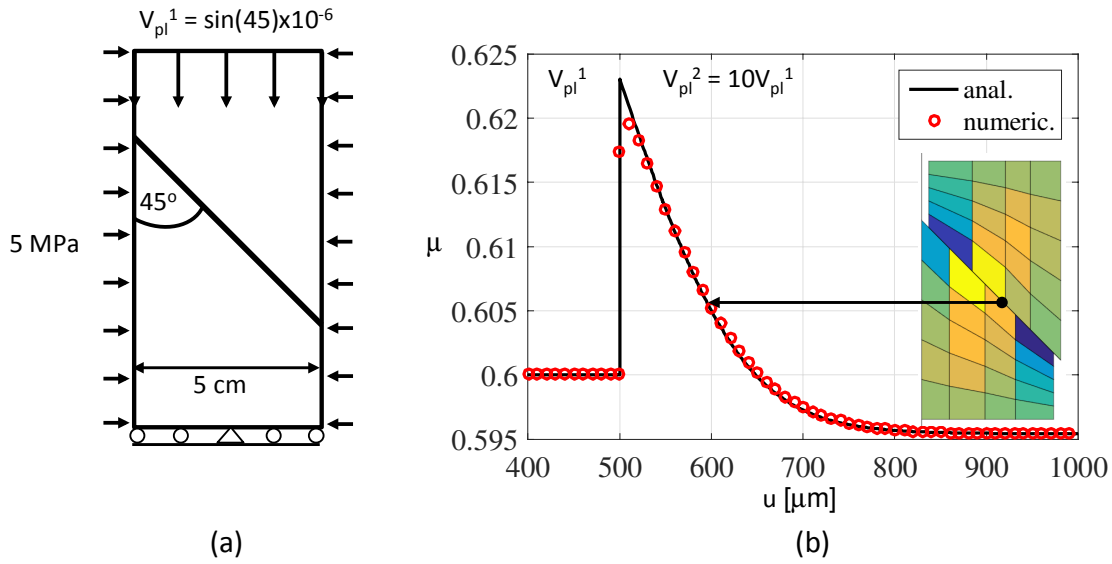

Figure 3. Benchmark problem for RS friction. (a) Geometry and boundary conditions. (b) Friction coefficient versus relative slip at the central node of the upper side of the fault in response to a change in the velocity of the upper edge and consequently the slip rate on the fault. The red circles represent the numerical solution, while the black line is the analytic solution. Note that we begin with a non-matching grid on the fault.

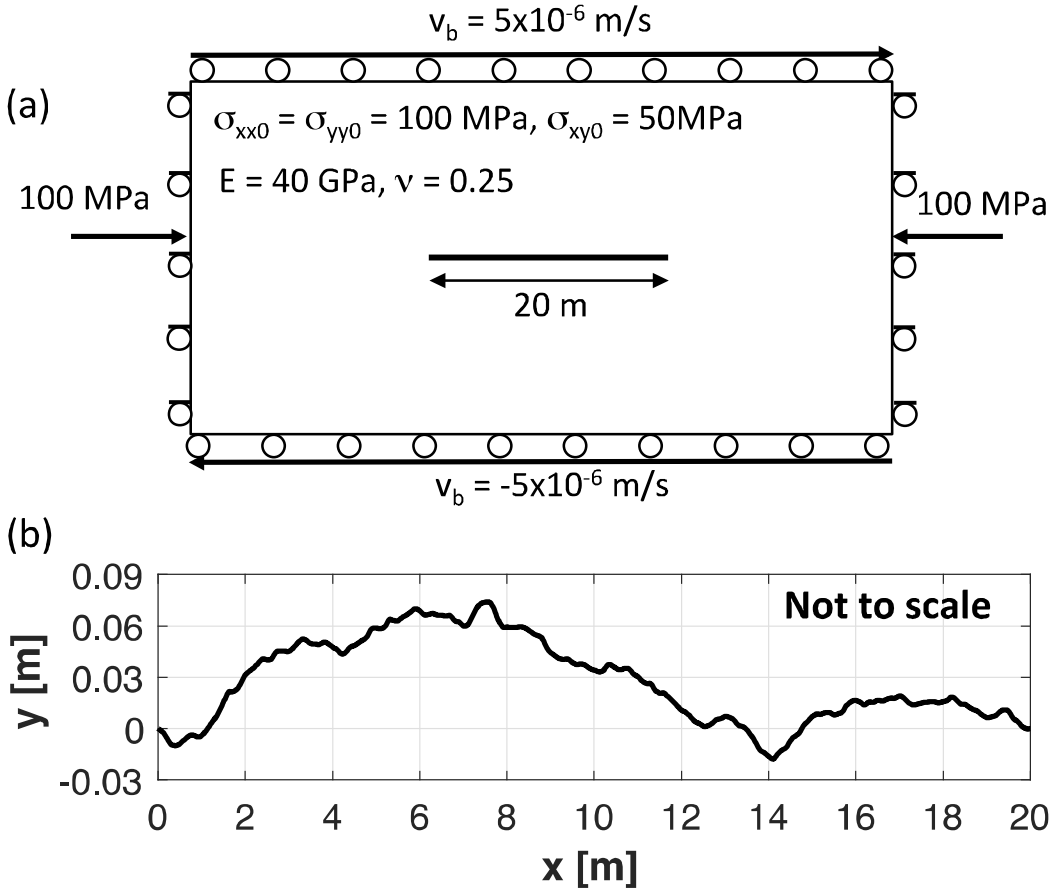

Figure 4. (a) The problem set up: a 60 x 30 m elastic medium with a 20 m long fault is subjected to a prescribed slow horizontal velocity $\pm V_b$ at the top and bottom and zero vertical displacements on all boundaries, resulting in a simple shear loading conditions. (b) The geometry of the fault: self-affine fractal roughness geometry with the minimum wavelength of roughness set to 20 cm.

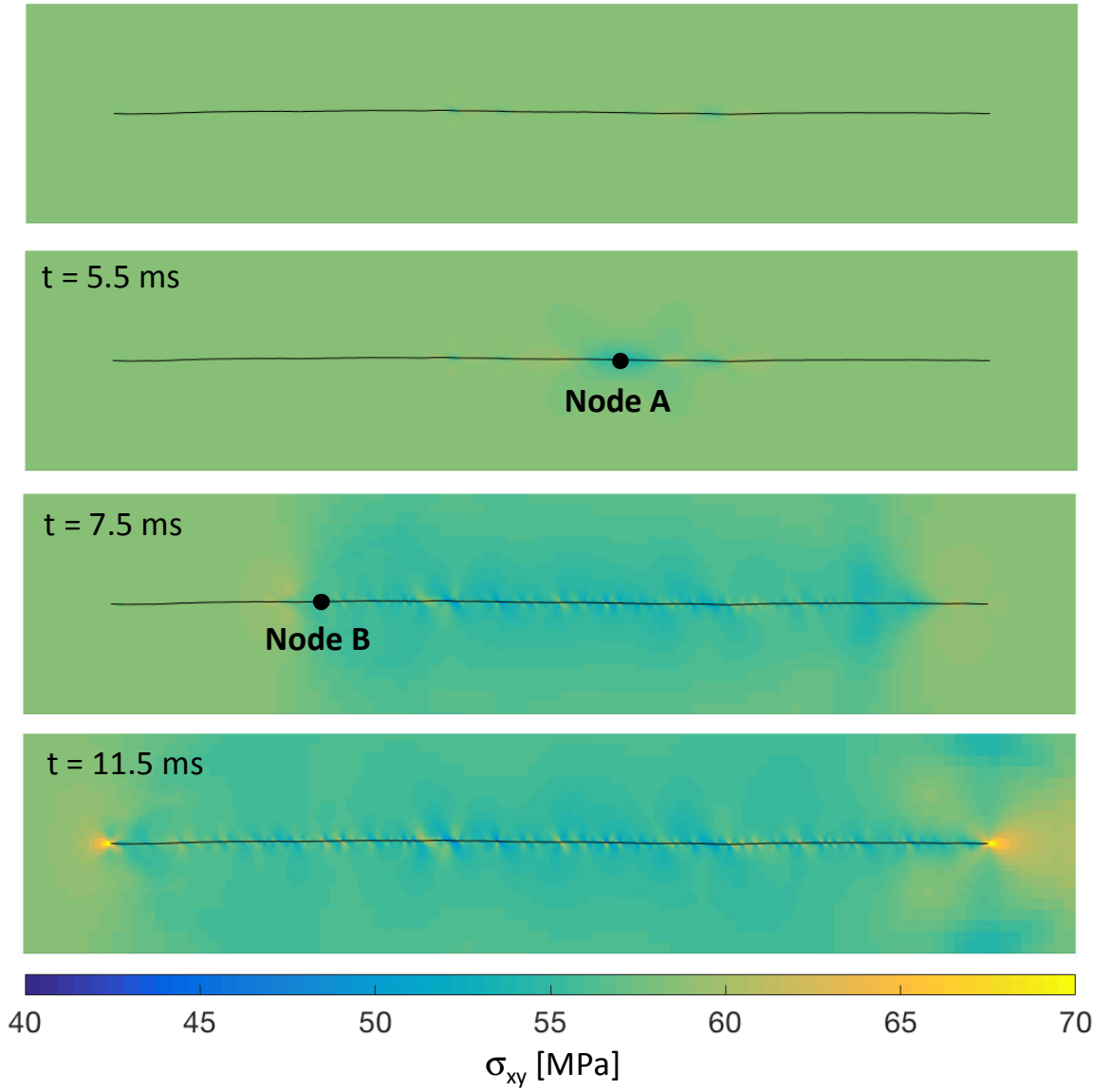

Figure 5. The distribution of shear stress around the fault at four different stages of a simulation with time discretization parameters of $\alpha = 1$, $\beta = 0.3$, and $\gamma = 0.6$. The reference for the time shown is the end the quasi-static loading stage (stage 1). The black circles show the locations where the sliding velocity and shear traction are measured in Figure 6. To show all the stages with the same color scale, we limit the values between 40 and 70 MPa.

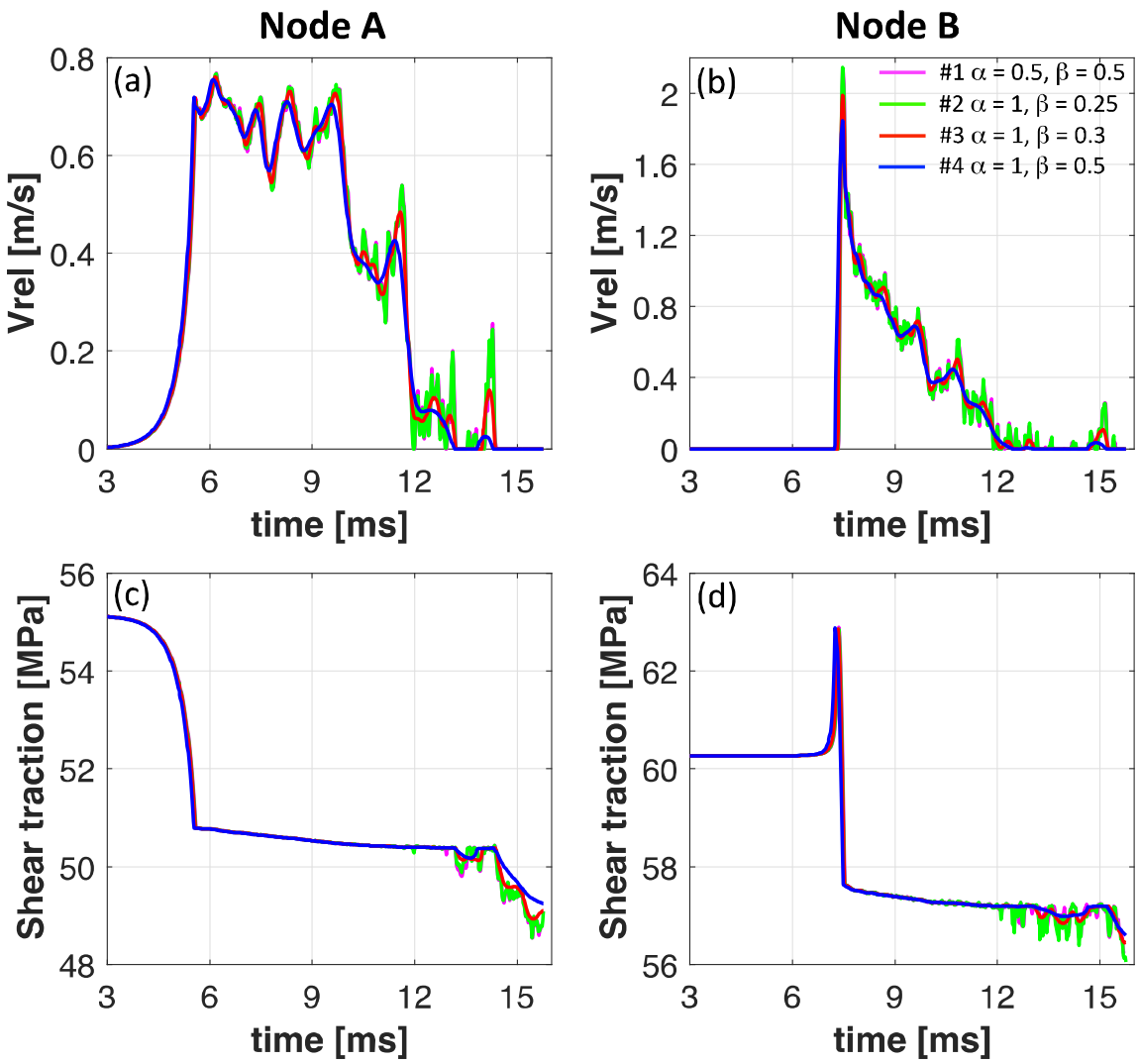

Figure 6. The effect of the time discretization parameters on the time evolution of sliding velocity and shear traction at nodes A and B for a fault governed by SW friction. The nodes are located inside and outside the nucleation region, respectively (see Figure 5). Note that in all schemes we choose $\gamma = 0.5\beta$ and the time is calculated from the end of the quasi-static loading stage.

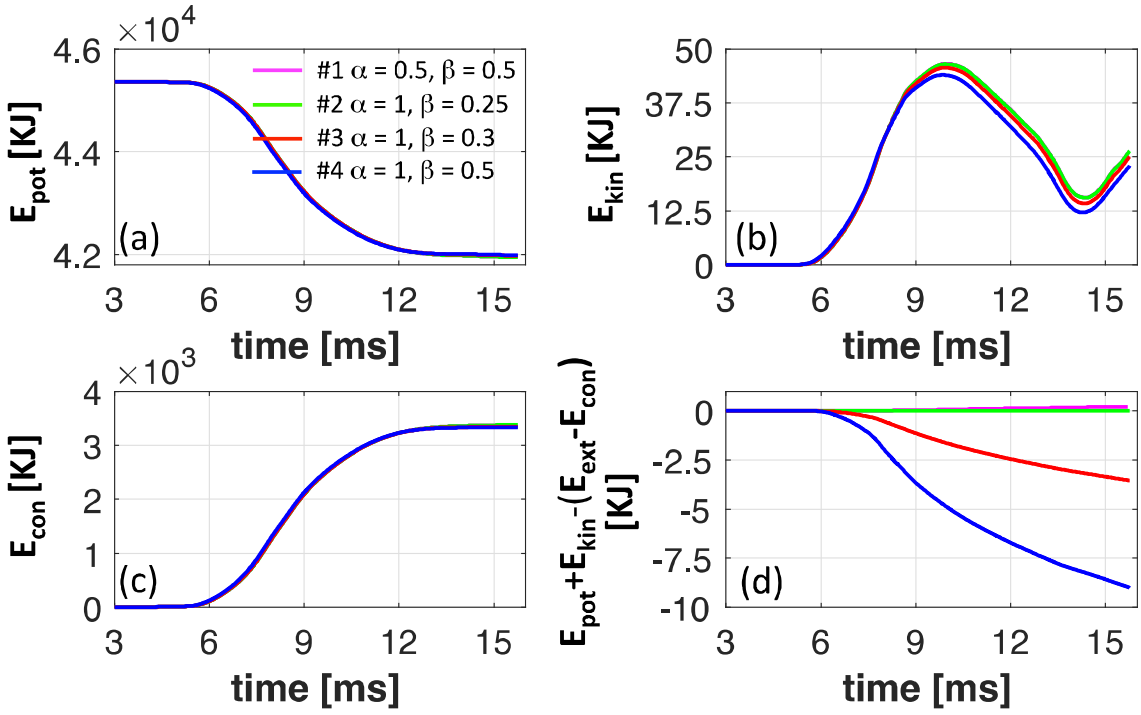

Figure 7. Potential (a), kinetic (b), contact (c), and the energy balance (d) vs. time for the four time discretization schemes. Note that in all schemes we choose $\gamma = 0.5\beta$ and the time is calculated from the end of the quasi-static loading stage.

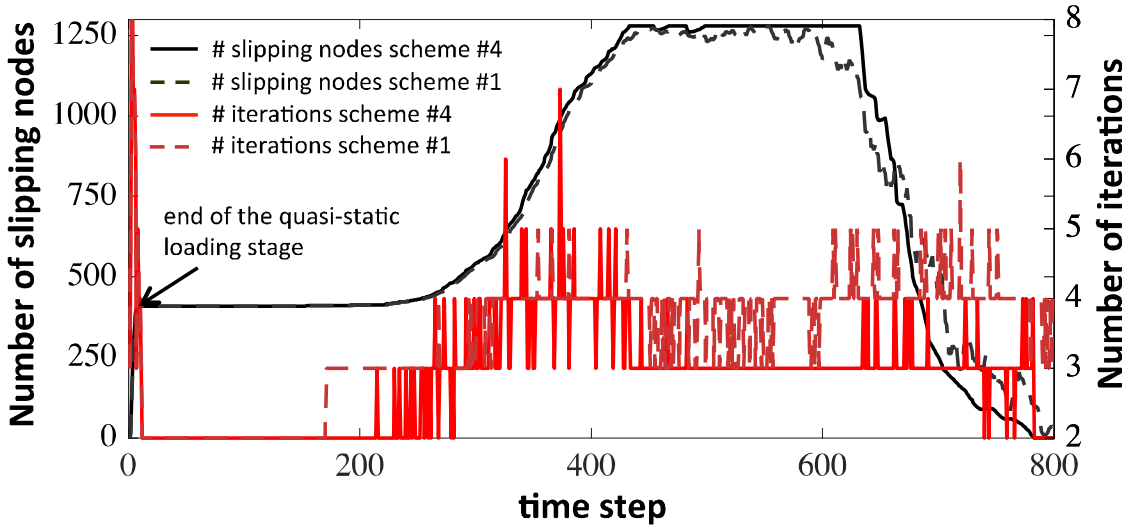

Figure 8. Number of slipping nodes (black) and iterations (red) during the simulation for scheme #1 (solid) and scheme #4 (dashed).

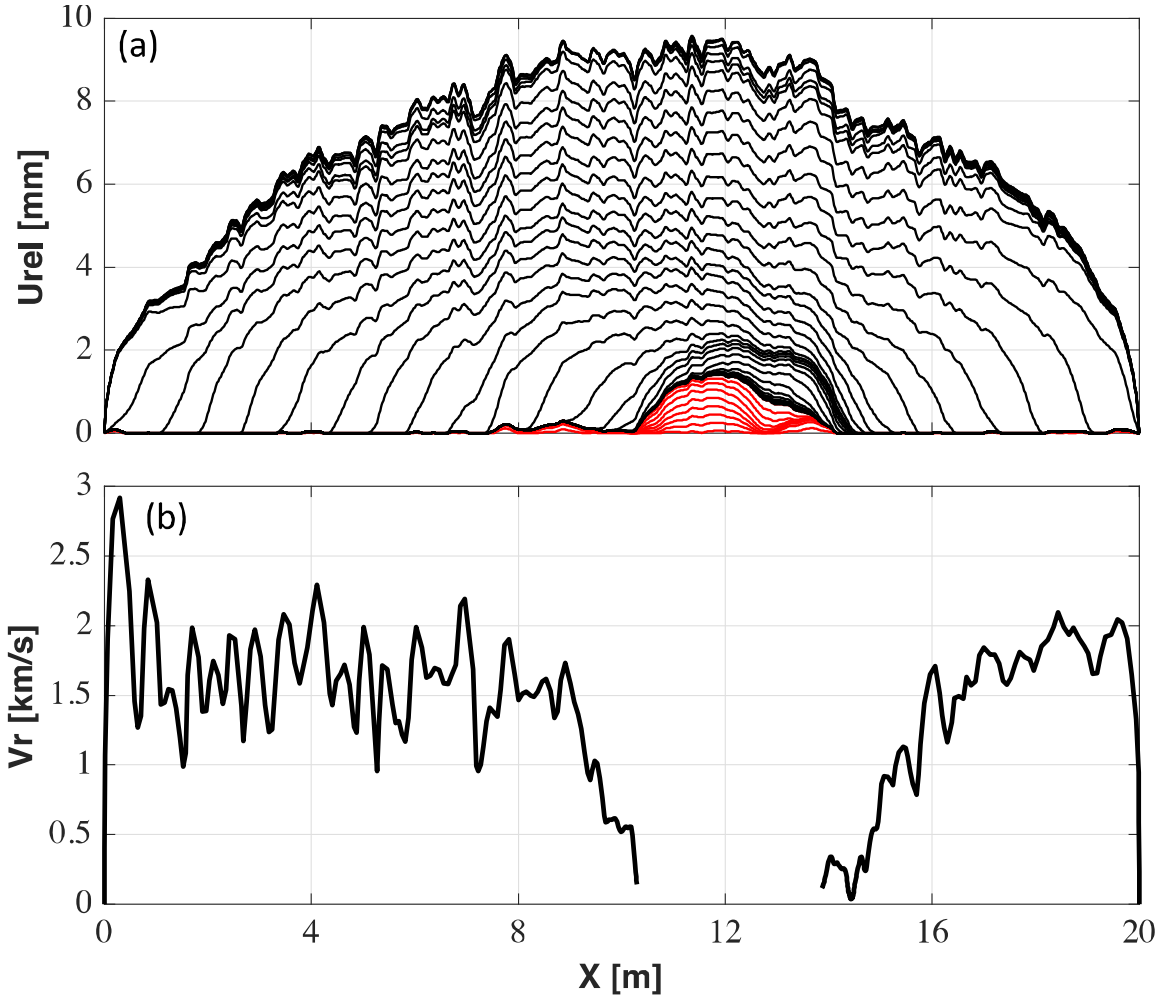

Figure 9. (a) The evolution of slip along the fault with time for a simulation with time discretization scheme #2. The initial quasi-static stage is represented by red contours, with decreasing time intervals between the contours, while the dynamic stage is represented by black contours with the time interval between the contours set to a value of 5×10^{-4} s. (b) The rupture velocity V_r along the fault.

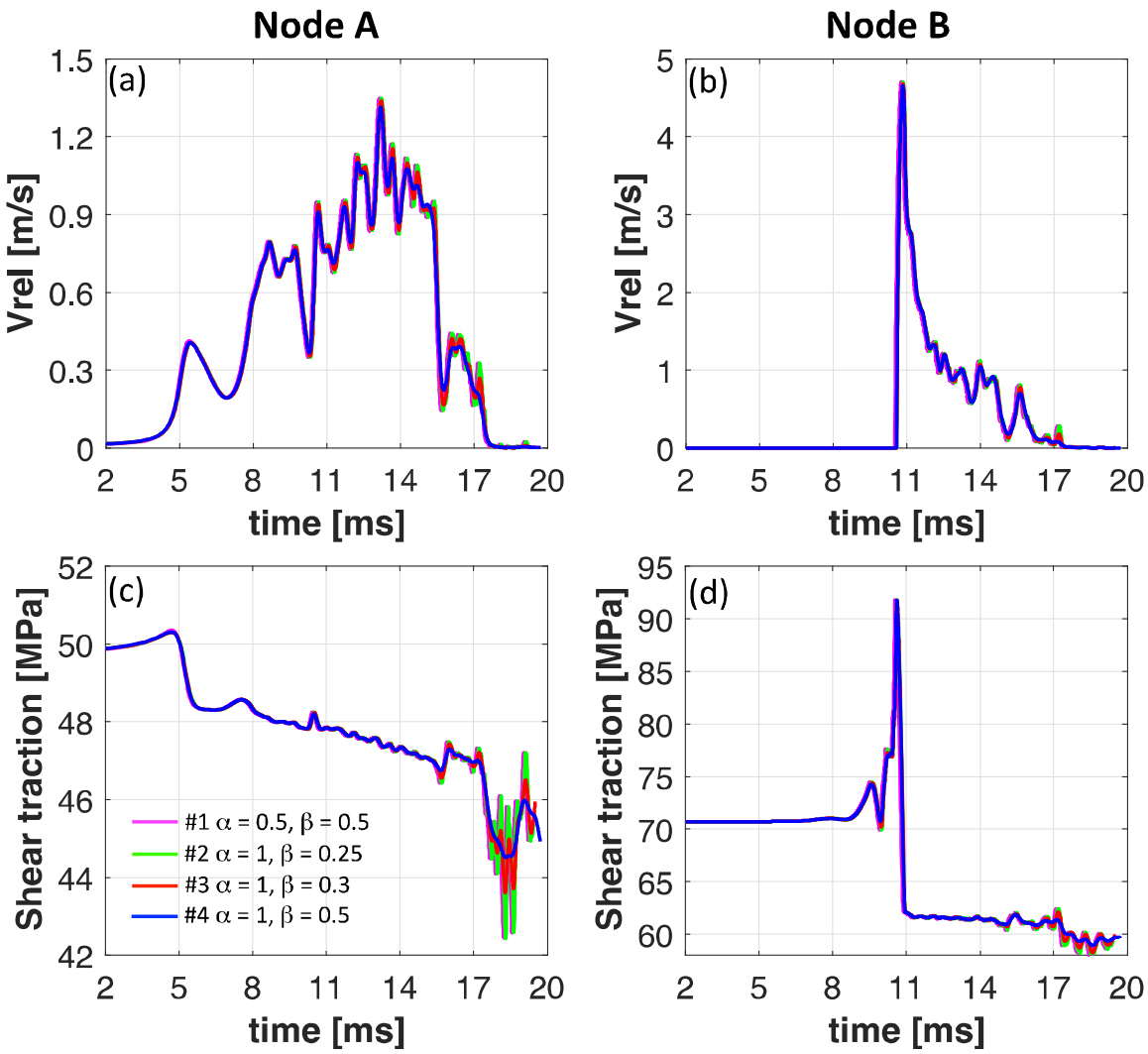

Figure 10. The effect of the time discretization parameters on the time evolution of sliding velocity and shear traction at nodes A and B for fault governed by RS friction. Note that in all schemes we choose $\gamma = 0.5\beta$ and the time is calculated from the end of the quasi-static stage.

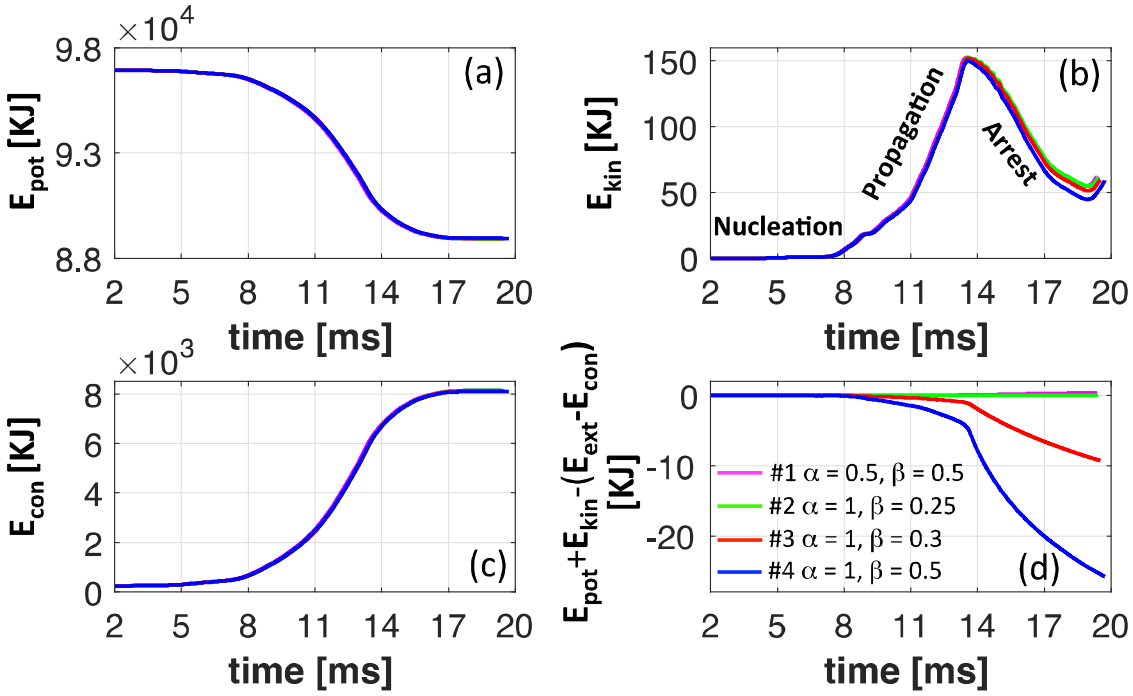

Figure 11. Potential (a), kinetic (b), contact (c), and the energy balance (d) vs. time for the four time discretization schemes. Note that in all schemes we choose $\gamma = 0.5\beta$ and the time is calculated from the end of the quasi-static stage.

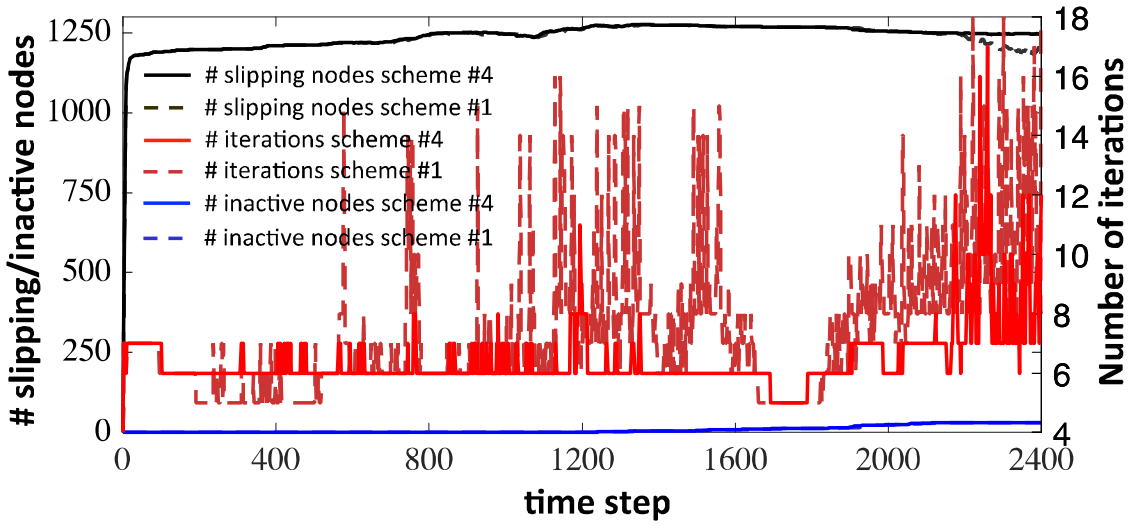

Figure 12. Number of slipping (black) and inactive (blue) nodes and number of iterations (red) during the simulation for scheme #1 (solid) and scheme #4 (dashed).